Research Square

Preprints are preliminary reports that have not undergone peer review.
They should not be considered conclusive, used to inform clinical practice,
or referenced by the media as validated information.

A 128-Channel Wireless Wearable Myolink (W2 Myolink): Functional Characteristics and Multidisciplinary Experiments

Maciej Zajaczkowski

maciej.zajaczkowski18@imperial.ac.uk

Imperial College London

Simos Koutsoftidis
Imperial College London

Muhammad Sheeraz
Imperial College London

Deren Yusuf Barsakcioglu
Imperial College London

Tianyu Jia
Imperial College London

Ciaran A McGeady
Imperial College London

Aritra Kundu
Imperial College London

Matteo Pizzi
Imperial College London

Fabio Tatti
Imperial College London

James Bashford
Kings College London

Patel Bhavesh
Imperial College London

Dario Farina
Imperial College London

Emmanuel Drakakis
Imperial College London

Research Article

Keywords:

Posted Date: April 28th, 2026

DOI: https://doi.org/10.21203/rs.3.rs-9266175/v1

License: This work is licensed under a Creative Commons Attribution 4.0 International License.
Read Full License

Additional Declarations: No competing interests reported.

A 128-Channel Wireless Wearable Myolink (W^2 Myolink): Functional Characteristics and Multidisciplinary Experiments

M.Zajaczkowski, S.Koutsoftidis, M.Sheeraz, D.Y.Barsakcioglu, J.Tianyu, C.A.McGeady, A.Kundu, M.Pizzi, F.Tatti, J.Bashford, P.Bhavesh, D.Farina, E.M. Drakakis

E-mail: maciej.zajaczkowski18@imperial.ac.uk, e.drakakis@imperial.ac.uk

Abstract. This paper presents Wireless Wearable Myolink (W2 Myolink), a high-density, battery-powered system for wireless acquisition of surface electromyography (EMG) signals, and demonstrates its practicality across diverse experimental paradigms. The device features a compact form factor (110×70×35 mm), low weight (160 g), and continuous operation for up to 6 h. It supports low-noise (1.34 µVRMS), high-resolution (24 bit) recordings from 128 EMG channels with real-time wireless data transmission over Wi-Fi. The capabilities of W2 Myolink have been validated through a series of experiments. Conventional EMG studies included the recording and analysis of muscle activity during various gestures and hand movements, as well as concurrent EMG–EEG measurements for the investigation of cortico-muscular coherence. The system's suitability for clinical and pathological scenarios was examined using surrogate EMG signals representative of healthy subjects and of conditions such as myopathy, neuropathy, and Amyotrophic Lateral Sclerosis (ALS). More complex experimental use cases involved human–robot interaction with ISYBOT robotic arms, intraoperative EMG monitoring during different types of surgery with and without exoskeleton assistance for the surgeon, and EMG acquisition during psychedelic experiences induced by psilocybin. Collectively, these results demonstrate that W2 Myolink can reliably acquire and wirelessly transmit high-quality, high-density EMG data in a broad range of research and application contexts.

1. Introduction

High-density electromyography (HD-EMG) recording is an enabling technology with significant implications in human robot interaction, neurorehabiliation, and human machine interfaces [1][2][3]. HD-EMG works by placing an electrode array with a large number of electrodes (32+) on the skin to record the muscle electrical activity, the electromyography (EMG), which is a convolutive mixture of motor unit activity.

This allows for the coverage of a larger skin area and thus more muscle activity to be collected cumulatively from each electrode site [4]. The spatial characteristics of the electrode locations allow for the application of spatial decomposition algorithms such as independent component analysis (ICA) and motor unit action potential (MUAP) decomposition of muscle activity and can enable the application of further algorithms for real-time MU tracking[5][6]. A large amount of electrodes also improves the likelihood that some will be in ideal locations for signal acquisition and thus overall, allow for complex mapping of muscle activity in complex dynamic tasks [7]. In addition, there is evidence that cortical activity can be detected in the beta band of EMG signals which presents an interesting application for peripheral brain-computer-interface (BCI) research [8].

Regrettably, research in the field is often limited by trade offs in existing devices; devices with high channel number tend to be bulky, expensive and come with a multitude of wires which add to clutter, impede the devices' practical deployment in experiments and interfere with natural behaviours and settings. In contrast, wireless wearable devices often have a low channel count, limited battery lifetime and poor noise performance [9] [10] [16]. This means that there is a range of experiments, conceived or conceivable, that would benefit from a miniaturised device which combines high channel count operation, high fidelity in EMG data acquisition and wearable characterisitics thanks to a low area profile.

The purpose of this paper is to illustrate the deployment in practical experimental settings of a new, advanced, battery-operated, wireless, wearable HD-EMG device henceforth referred to as the W^2 Myolink, to demonstrate its capabilities and highlight the implications of such a development within the context of the growing fields of neurotechnology and wearable devices. We aspire to portray how we conducted some challenging experiments, and expand on the usefulness of the findings and the device itself to researchers from different fields. The paper is organised as follows: in Part 2, the new wireless wearble myolink device is presented whereas Part 3 lists a series of experiments conducted by means of the new device. We present customary and complex experiments; the customary experiments involve basic gesture recordings, EMG-EEG coherence test, real time motor unit decomposition and the playback of ALS, neuropathy myopathy data while the more complex experiments involve, human robot interaction, the effect of an exoskeleton on surgeon' muscle fatigue in surgeons and psychedelic experience monitoring.

In addition, we aim to show progressive testing of the device and its transition from simple electrical testing to full scale experiments. With this, we aim to convey structure and logic to the experiments and outline a framework that others may also use when testing their own novel devices. As such, the paper peaks with complex experiments exploiting the opportunities arising from the wireless, wearable and portable properties

of the device.

1.1. Methods

The wireless wearable Myolink (W^2 Myolink) presented here constitutes a progressive trade-off with respect to research and commercial state of the art devices. As detailed in [12], the W^2 Myolink is optimised to satisfy multiple features at the same time including a high number of channels, low area profile, high recording and transmission fidelity and high signal to noise ratio (SNR). In addition to being wearable, the W^2 Myolink device is also portable, efficiently fitting into a pelican case along with a small bag for electrode preparation supplies. Unlike other commercially available devices characterised by a sizeable receiver base which renders transportation cumbersome, the W^2 Myolink can be safely and conveniently transported and deployed into a variety of environments including operating theatres and a variety of labs, for example those involving robotics, neurorehabiliation and even neuropsychopharmacological studies.

Figure 1 illustrates the W^2 Myolink while Figure 2 illustrates the same device along with its peripherals (electrodes and other practical components for deployment). Figure 4 exemplifies how W^2 Myolink can be worn when, for example, one is interested in HD-sEMG recordings from the lower part of the right arm. Table 1 summarises the functional and physical characteristics of the W^2 Myolink and two other competitive commercially available devices from Bioelettronica. Referring to Table 1, it becomes clear that the new device is designed in such a manner that it trades off key characterisitics with respect to the two commercial devices. Compared against Quattrocento [9], which offers an impressive count of 400 wired channels (albeit at the expense of high weight and increased size), the W^2 Myolink offers 128 wireless channels benefiting from a lower Input Referred Noise (IRN), much less weight and higher bit-depth. Compared against Muovi [10], the W^2 Myolink offers double the count of wireless channels, lower IRN, higher bit depth, and longer battery operation. On the other hand, the size of the W^2 Myolink is slightly bigger than the size of the Muovi wireless node, but the wearability of the new device is still perfectly and conveniently possible. From the above comparison it is plausible to argue that commercially available devices are designed for two extremes of range of use: one offering a very high number of EMG channels while the other offering as small the size of a wireless EMG node as possible. On the other hand, the new device represents an optimisation which sits between the two extremes above and combines a fairly large number of channels without sacrificing wearability, portability and practicallity.

The new device is accompanied by a set of electrodes for interfacing with the human body. Those electrodes (see Fig. 3) can be either commercially available (e.g. the Bioelettronica GR08MM1305 and GR10MM0808) or custom made. In addition, the W^2 Myolink benefits from also customised flexible lightweight extension cables which

can be attached to the new device alllowing for both integration with existing parts in the market as well as the adoption of new setups and interfaces that are not currently available on the market.

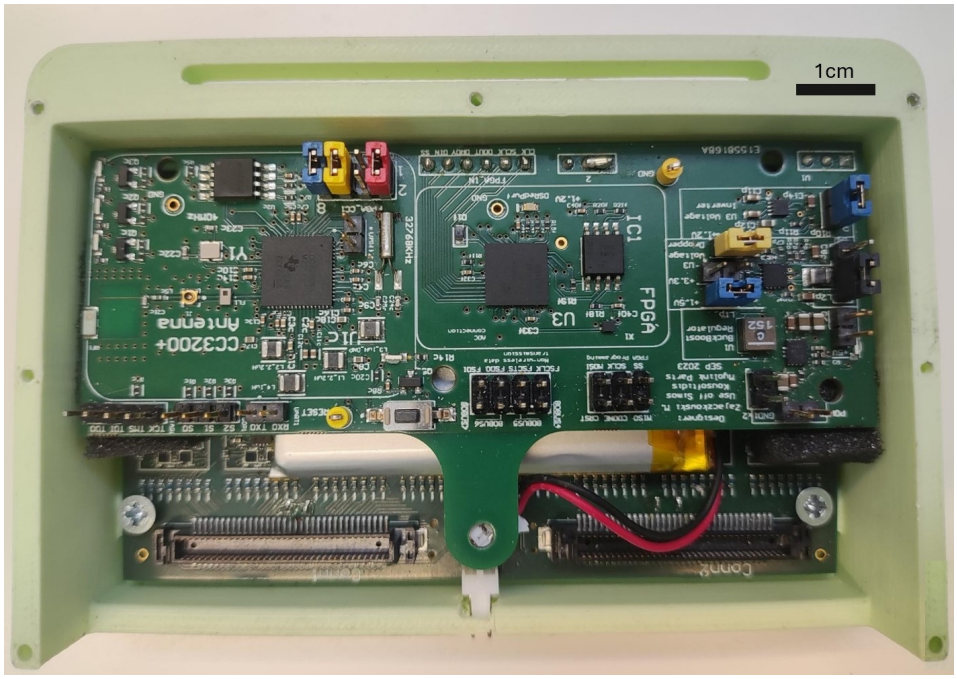


Figure 1. The W^2 Myolink comprises two boards: one comprised of electrode sockets, analog front ends (AFEs) and analog to digital connectors (ADCs) for acquiring EMG signals, and one comprised of the power supply level, ICE40HX8k FPGA and the CC3200 WiFi microcontroller for processing and transmitting the data. Both boards were joined together and neatly placed into a low profile 3D-printed box with slots on the sides to faciltate secure attachment to the body through waistband elastic strip. Full technical details and characterisitcs of the new device are provided in 'A Wearable 128-Channel Wireless Device for High-Density Surface Electromyography Recording' [12].



Figure 2. The W^2 Myolink and its peripherals within their briefcase (0) 128 channel custom flexible PCB electrode grid, (1) Custom flexible PCB 20cm extension cables (2) Router power cable and tape, (3) WiFi router for data transmission, (4) The electronics of the W^2 Myolink (see also Fig. 1) encased in plastic box, (5) Electrode connector breakout test board (for breaking out individual input channels), (6) Bandage for securing electrode grids, (7) Battery charger, (8) Flexible waistband elastic strip, (9) Battery voltage control charge circuit.

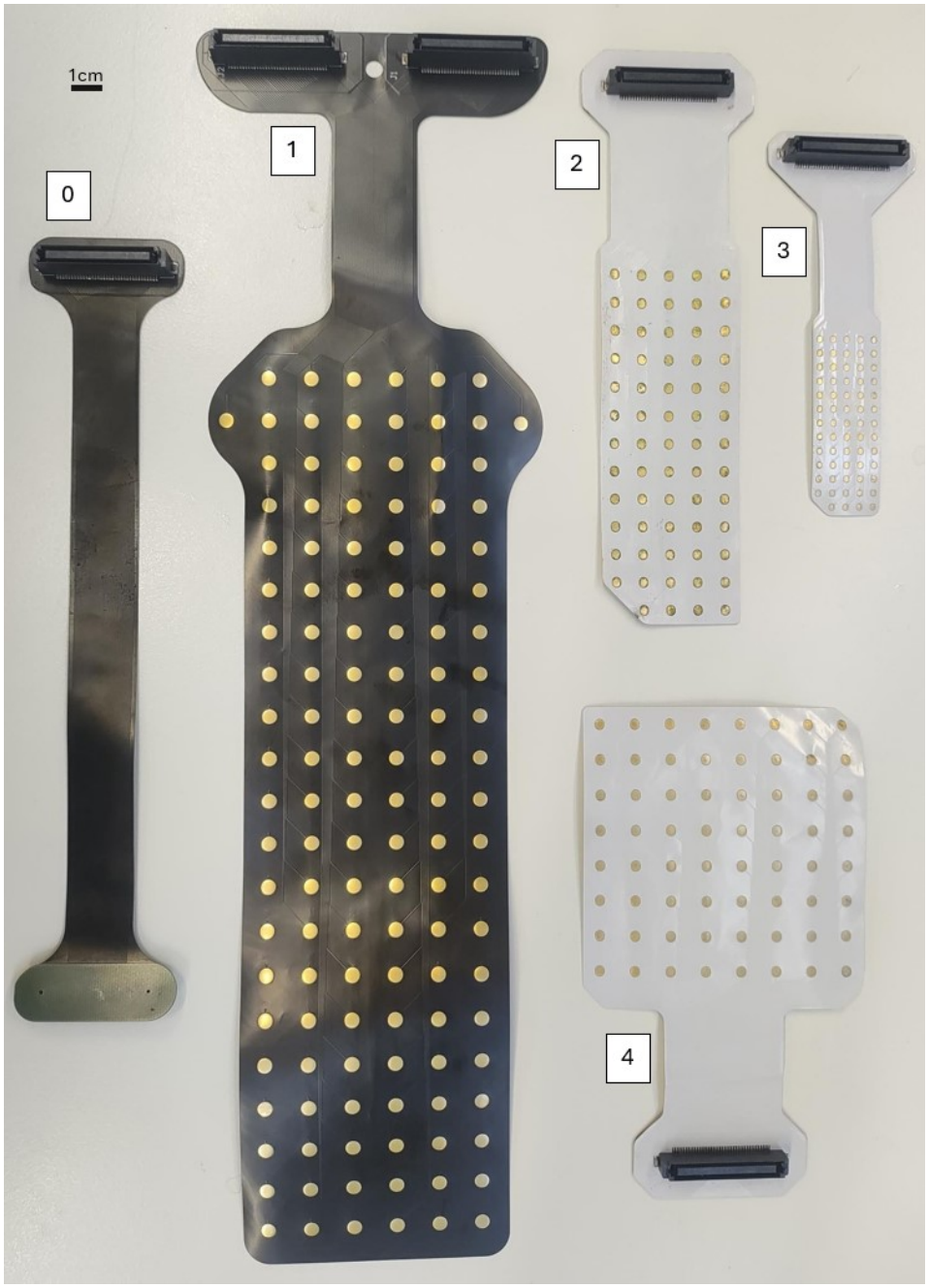


Figure 3. The range of commercial and customised electrodes used with $W^2Myolink$. All designs follow the same flexible PCB design with FR4 material stiffener reinforcing the KX14-70KXDE (where X is the component height) connector to maintain a robust interface with the W^2 Myolink. For an element wise breakdown: (0) A 20cm extension cable. The opposite gender connector (KX15-70KXDE) is located on the flip side of the FR4 material (green) which enables the stacking of cables. (1) A 128-channel custom electrode grid with a 12mm inter electrode distance (IED) and 6*21 arrangement used for acquiring EMG data from the back of surgeons during live surgery as illustrated in section 4.4. (2) Bioelettronica 64 channel GR08MM1305 electrode grid with an 8mm IED and 5*13 electrode arrangement. (3) Bioelettronica 64 channel GR04MM1305 grid with an 4mm IED and 5*13 electrode arrangement (4) Bioelettronica GR10MM0808 grid with 8mm IED and 8*8 electrode arrangement. All electrode grids were fitted with a foam stencil and covered with conductive gel before application to skin. [13]



Figure 4. The W^2 Myolink "worn" by a subject and covering the lower part of the right arm.

Table 1. Comparison of the characterisitics (column 1) of two commercially available OT Bioelettronica devices (columns 2 and 3) with the W^2 Myolink (column 4). Although the OT Bioelettronica market devices surpass the W^2 Myolink in some aspects, they are often optimised for a narrow range of characterisitics such as low area profile or high channel count whilst trading off for wirelessness and current consumption, or bit-depth and bandwidth. In contrast, the design of the W^2 Myolink attains a balance of a high number of channels, low input referred noise, and low area profile whilst also being wireless, wearable and maintaining a high radio link quality, single charge use time, bit-depth and sampling rate.

Table	Bioelettronica Quattrocento [9]	Bioelettronica Muovi+Pro [10]	$W^2 Myolink$
Wireless	No	Yes	Yes
Wearable	No	Yes	Yes
Portablility	No	Low	Yes
Channel number	400	64	128
EMG Bandwidth	0.7-4400Hz	10-500Hz (selectable)	16-430 Hz
Sampling Rate	512-10240Hz	2000Hz	2000Hz
Front End Power Supply	5V	3.3V	1.5V
Max Input Value	33mV	18.75 to 150mV (setting dependent)	7.5 mV
Front End Gain	43.5dB	Not Reported	46dB
EMG Bit Depth	16	16	24
Radio Link Quality	N/A	Not reported	99.7%
Wireless Protocol	N/A	WiFi	WiFi
Current Consumption	1667mA	162mA	280mA
Input Referred Noise	Less than 4000 nVrms	less than 4uVrms	1340 nVrms
Size/Area Profile (Whole device)	395x271x130mm	49x45x18 probe (station (178 x 178 x 29 mm))	110x70x35mm
Weight	5kg	2*42g (with base station 725g)	160g
Single Charge Use time	N/A	2.5hrs	6-7hrs

2. Experiments

The experiments section is divided into two parts; customary and complex experiments. The former relates to typical testing of the device while the latter relates to full deployment of the W^2 Myolink in experiments it can enable.

3. Customary Experiments

This section describes experiments that may not fully take advantage of all the features of the W^2 Myolink, yet are crucial in demonstrating the functionality of the device in real-life settings whilst displaying the diversity of experiments the W^2 Myolink can enable.

3.1. Finger Pressure, Fist Clenches

Recording of the neuromuscular signals from the forearm while performing hand gestures is a common method for testing the functionality of HD-EMG system and is often used as a 'gold standard' in related publications [14][15]. The result is an elegant way to demonstrate the functionality of each individual electrode, to portray a clear 2D map of muscle activity, and to map the activity from a set of complex muscle structures in the forearm [16].

For this experiment, 128 channels of EMG were setup in a similar way as in Figure 6. Figure 5 illustrates the unprocessed HD-EMG recordings from 64 channels against time when the device is arranged as shown in Fig. 6 as a verification of signal quality with the smoothness of the unprocessed signals manifesting the quality of the recording setup. Although, from a brief overview of the figure, some channels appear redundant, with spikes of activity repeating across channels, this is actually indicative motor unit action potentials originating from under specific electrodes (where the spike amplitude it highest) propagating across space and being detected in other channels with a lower amplitude and with a small time delay. Upon closer inspection we can also observe that there are significant differences in the shape of these spikes of activity suggesting unique information is contained in the data recorded.

In Figure 7, one can observe random activity in the rest condition, and spread high muscle activity when making a fist (which involves multiple muscles at high force). Other unidirectional hand movements appear as patches of activity constrained to specific groups of electrodes. On the other hand, Figure 8 shows finger lift movements; milder muscle activity differences across electrodes are observed. It is worth noting that this customary experiment demonstrates the importance of grid placement. More specifically, observing the last two columns in the patterns of muscle activity presented in Figure 8, not much of the activity is picked up due to finger movement.

To conclude, first simple experiment succeeds in demonstrating the capability of the device to detect distinct patterns of activity from various gestures.

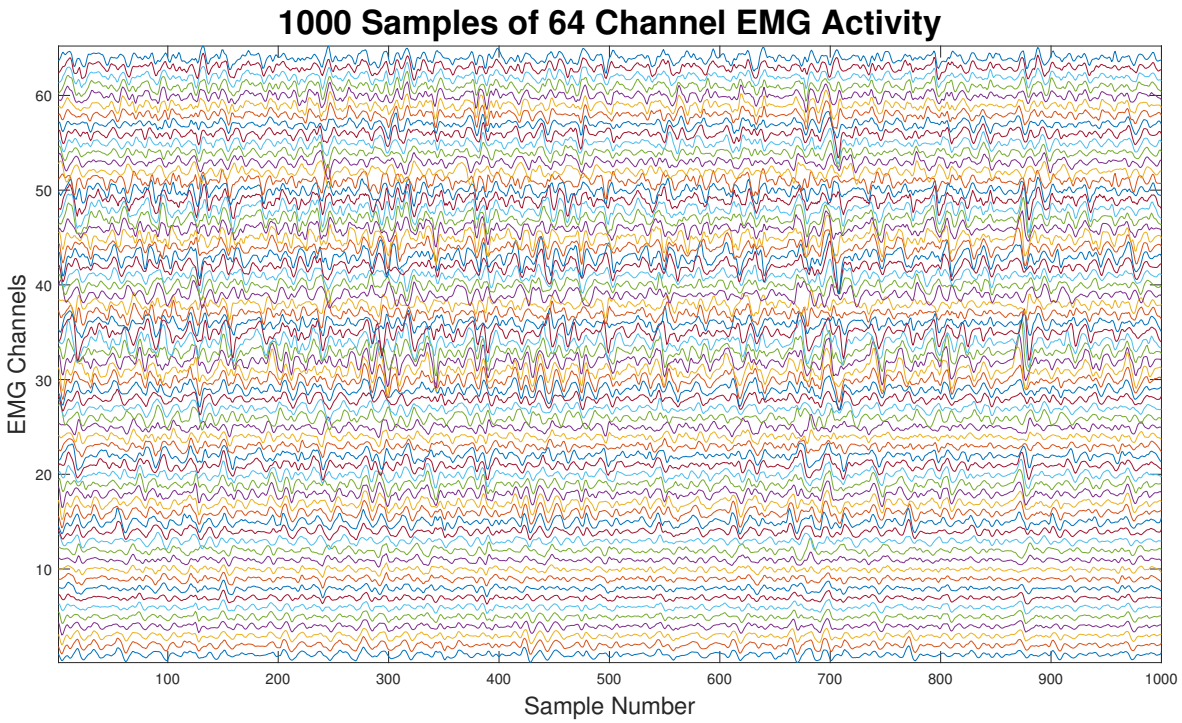


Figure 5. Example of 64 channel HD-EMG signals obtained by means of the W^2 Myolink during a simple gesture. The 1000 samples per channel shown corresponds to a duration of 0.5 seconds. The device is deployed on the upper limb as shown in Figure 6. The recorded data are raw (not post-processed); their smoothness and identifiable MUAP spikes manifest the quality of the recording setup. For reference, the quotient of the peak signal to the rest activity is 3.776.

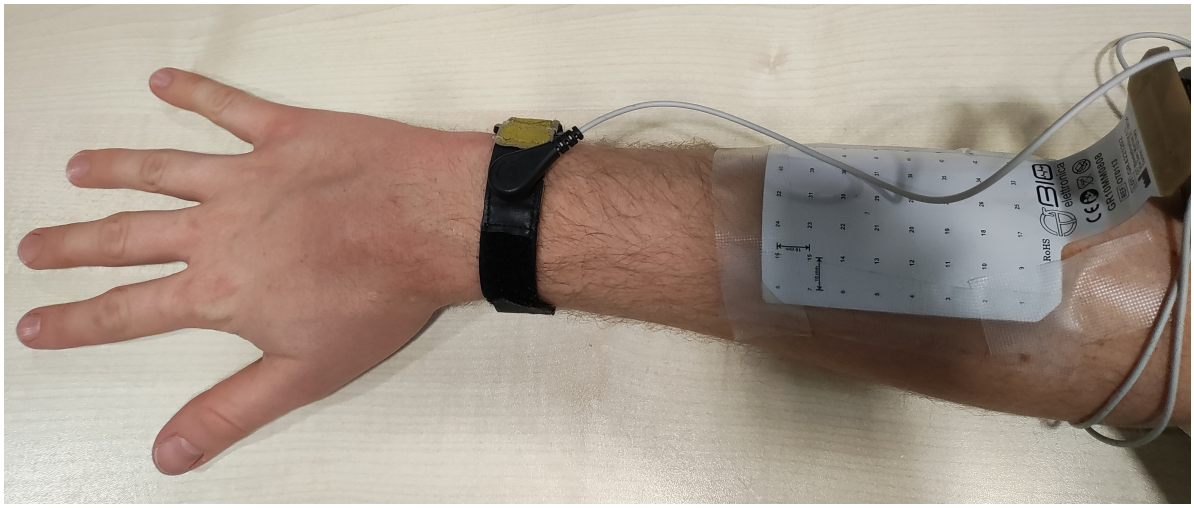


Figure 6. Sketch of the experiment specific deployment of the device on the upper forearm using a single 8*8 EMG 64 channel electrode grid of the same product series as the 5*13 electrode employed in this experiment. The setup illustrates a black wet wrist band grounding electrode and the white electrode grid with connectors to the device located on the upper forearm. The position of the electrode enabled the detection of muscle activity from forarm muscles relevant to finger and wrist movements.

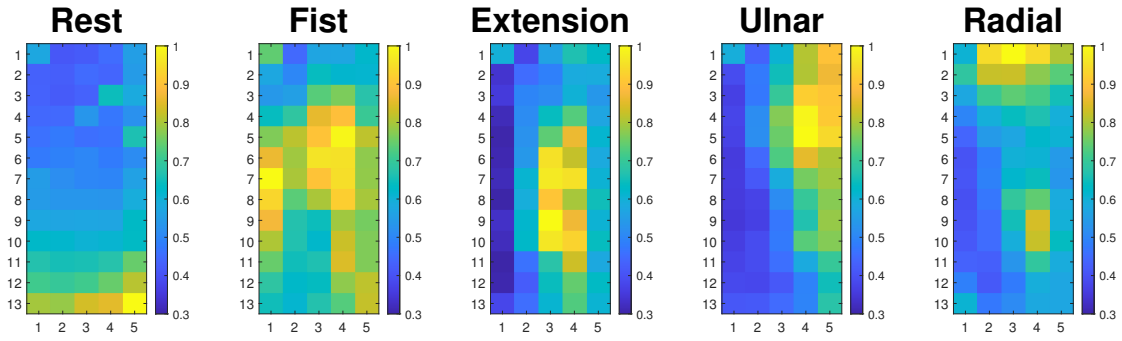


Figure 7. Mean absolute power of muscle activity when different gestures are performed. Notice the distinct patterns of activity corresponding to specific gesture related muscle contraction with mean RMS values of 57.3, 95.6, 231.0, 76.2, 144.8 microvolts for Rest, Fist, Extension, Ulnar and Radial movements respectively. Note that a large yellow region presented in the muscle activity maps, representing high values, indicates a broad peak but does not indicate its absolute magnitude due to the normalisation present in the colormaps.

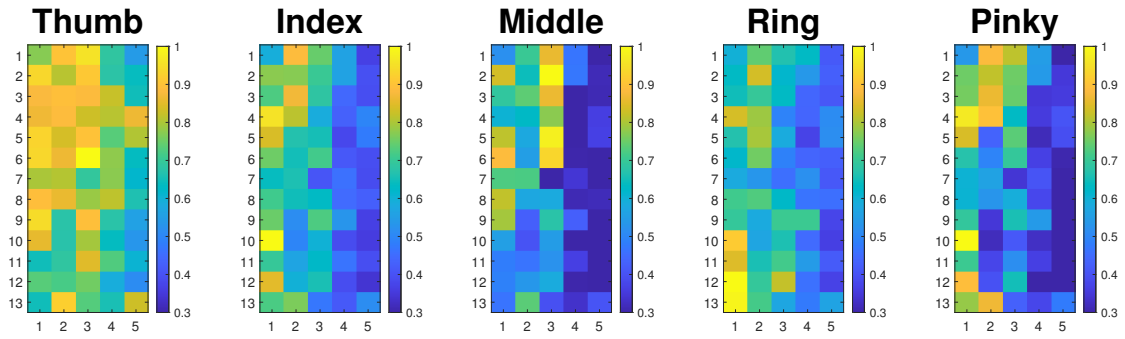


Figure 8. Mean absolute power of muscle activity when pressing down with each finger and maintaining pressure with mean RMS values of 65.8, 70.0, 85.1, 52.1, 59.5 microvolts for Thumb, Index, Middle, Ring and Pinky finger movement respectively.

3.2. EMG-EEG coherence test

Although not wireless, dual EMG-EEG studies are an emerging field in neuroscience and neural engineering. Such experiments allow a more integrated study of the motor nervous system, both peripheral and central, potentially allowing for better neurorehabilitation strategies and even peripheral brain computer interfaces. This, in turn, would enable various advantages including a more seamless interaction between humans and machines, better understanding of neural input from the brain to the hand and possibly better diagnosis of where damage has occurred in case of dysfunction (i.e. peripheral damage, spinal injury or brain damage) [17][18][19].

In this study, high-density surface EMG signals were recorded from the dominant wrist extensor muscle of an able-bodied participant using the $W^2Myolink$ system (Figure 9). The participant modulated force output from the extensor muscles via a force sensor to track an on-screen ramp profile, with the full experimental setup depicted in Figure 10. Twenty repeated ramp contractions were performed during simultaneous EMG and EEG recordings; each trial lasted 14 seconds, featuring a 10 second plateau at 10% of maximum voluntary contraction (MVC). A photocell positioned on the screen delivered a synchronisation trigger to the EEG amplifier's trigger port and channel 1 of the $W^2Myolink$. The EMG electrodes were arranged in a compact grid along the forearm muscle (Figure 10). EEG data were acquired using an actiCAP electrode cap (brain Products, Germany), an actiCHamp Plus amplifier (Brain Products, Germany), and BrainVision Recorder software.

Following the concurrent recordings of EMG and EEG signals, sampled at 2kSPS and 1kSPS (with cut off 62.5Hz) respectively, Figures 11, 12 and 13 were generated from calculating the cortico-muscular coherence using the signal.coherence function in Python. Referring to Figures 11 and 12; with electrodes adjacent to the left motor and premotor cortices (C3 and CP3 according to the 10-10 64 channel EEG setup), it can be observed that there is increased coherence in the high beta band (around 18 to 26Hz) which agrees with findings of [19]. Conversely, Figure 13 depicts the coherence from an electrode over the right motor cortex which controls the left hand and shows no such activity. This is expected as the task was performed with the right hand. Based on the coherence patterns observed against frequency, a scalp plot illustrated in Figure 14 was produced which depicts the coherence across all electrodes at 20Hz which is located in the middle of the beta band which is relevant to motor control. It is clear from this scalp plot that the cortico-muscular coherence value is higher on the left side which controls the right hand.

In conclusion, the W^2 Myolink was successfully deployed to demonstrate the connection between the muscle and brain, potentially opening opportunities for next steps involving neuromuscular coherence applied to sophisticated experiments with complex dynamic

motion. This would transform the current customary experiment into a complex experiment, possibly deploying EEG along with the W^2 Myolink in experiments such as ISYBOT human robot interaction presented in following sections of this paper.

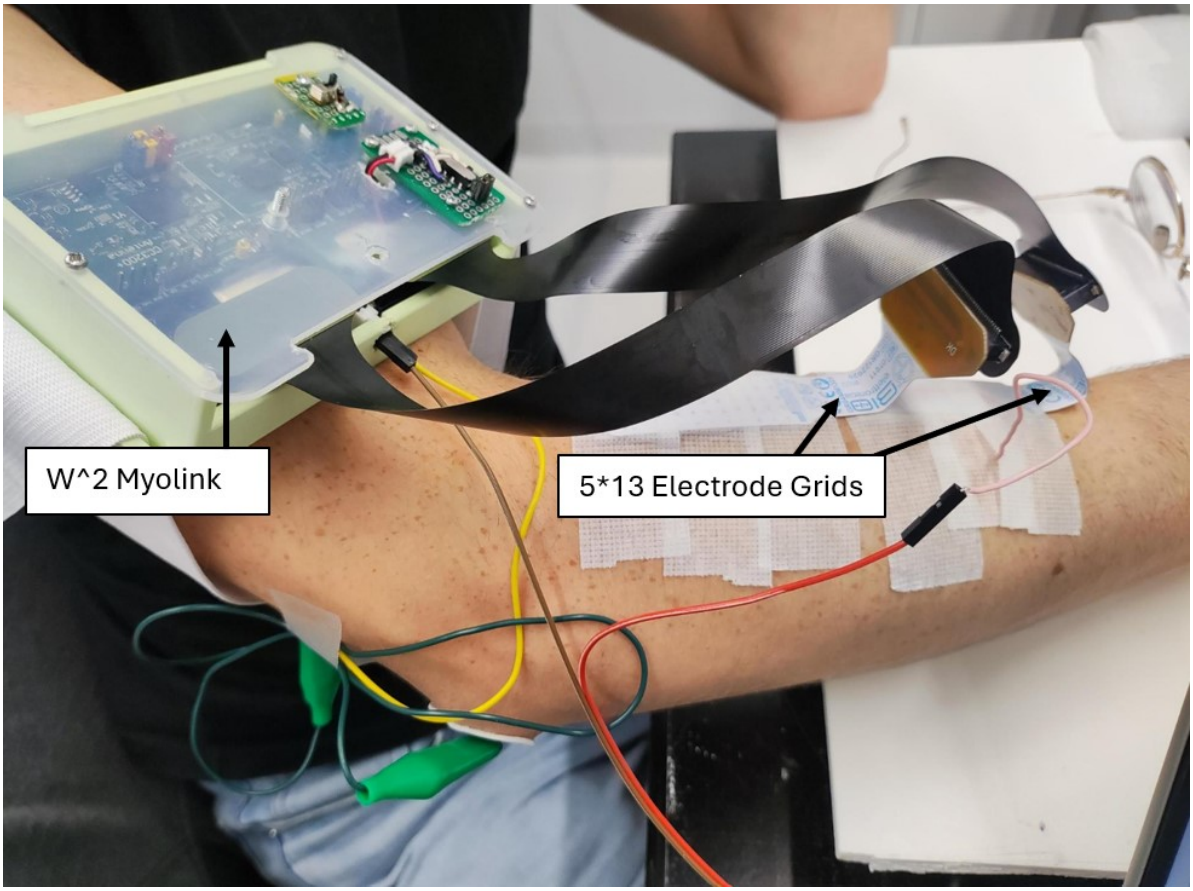


Figure 9. Close up view of how the device and the electrode grid set up were deployed. Two standard 4mm interelectrode distance 5x13 (64) channel electrode grids (Bioelttronica GR04MM1305) were placed on the forearm. The green and yellow cables connect the grounding electrode to the device and the red and pink wires connect the synchronisation signal (experiment trial start and trial stop) to the synchronisation input on the device. This input temporarily overwrites channel 1 of the device which indicates start and stop for each trial.

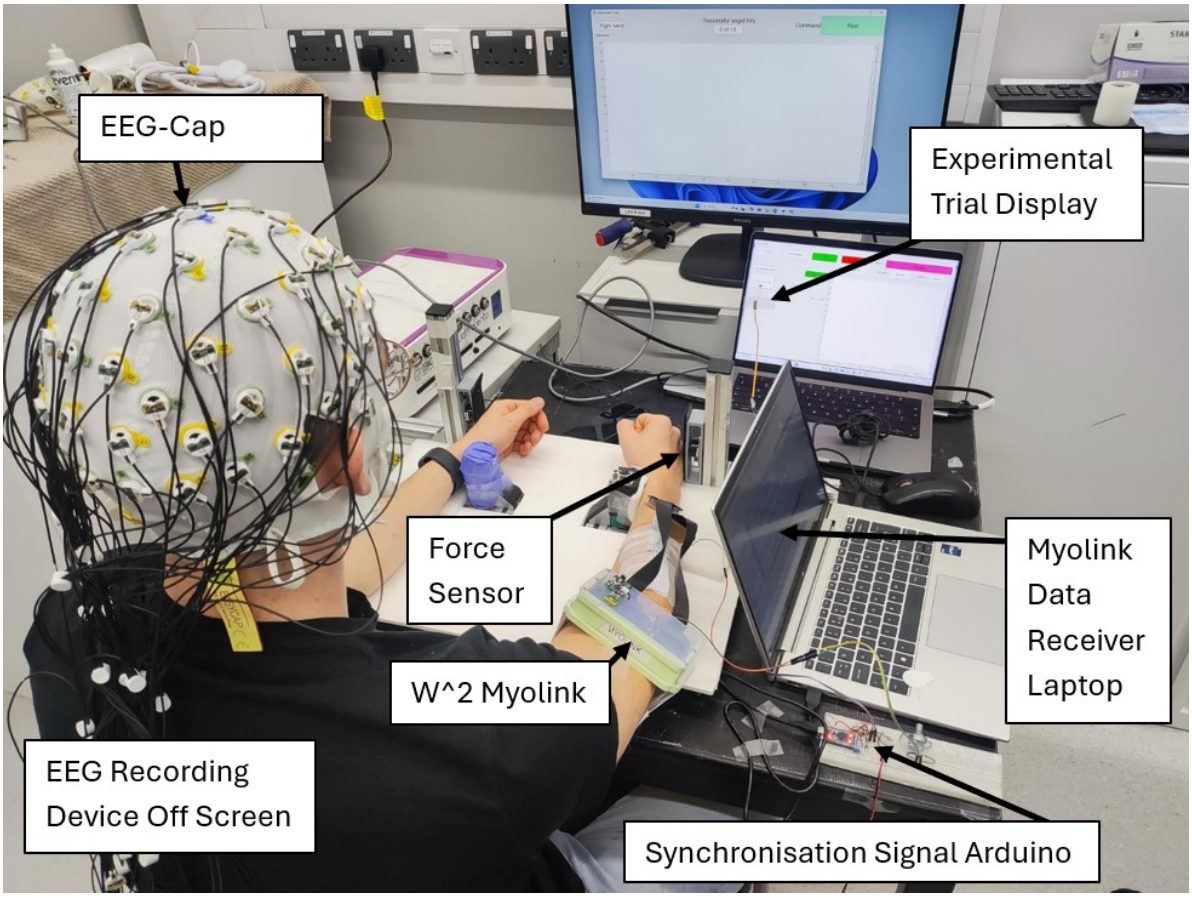


Figure 10. Full setup comprised of the EEG cap, $W^2 Myolink$, force sensor, experimental trial stimulus display, W^2 Myolink EMG data receiver laptop and synchronisation signal Arduino as labelled above. It should be noted that although the cap and EEG electrode setup is complete, only 18 electrodes were used; specifically the C, CP and FC electrodes according to the 10-10 64 channel EEG setup, only in the regions of interest to detect motor and premotor cortex activity. EEG Setup involved the EEG cap (actiCAP, BrainProducts, Germany) and the actiCHamp Plus amplifier (BrainProducts, Germany) along with BrainVision Recorder software for the recording of EEG.

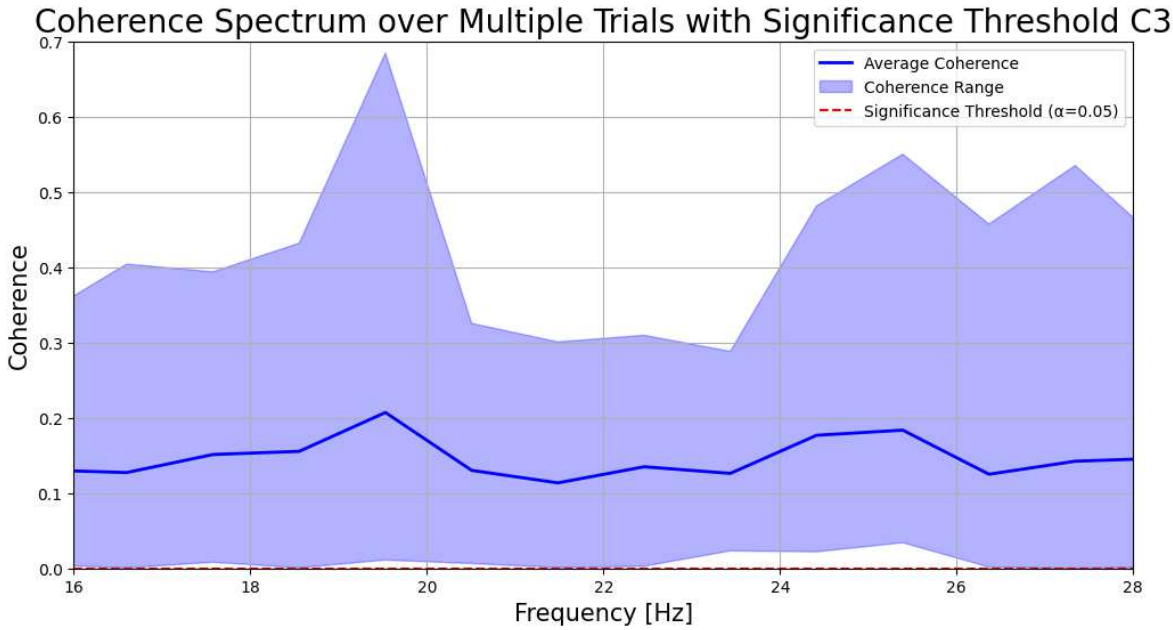


Figure 11. Cortico-Muscular Coherence peaks in the upper beta band region for C3 electrode which is adjacent to the left motor cortex. Since this brain region controls the right hand, which is active, the corresponding activity is as anticipated. Alpha (α) represents the significance threshold of 0.05 above which coherence values are statistically significant.

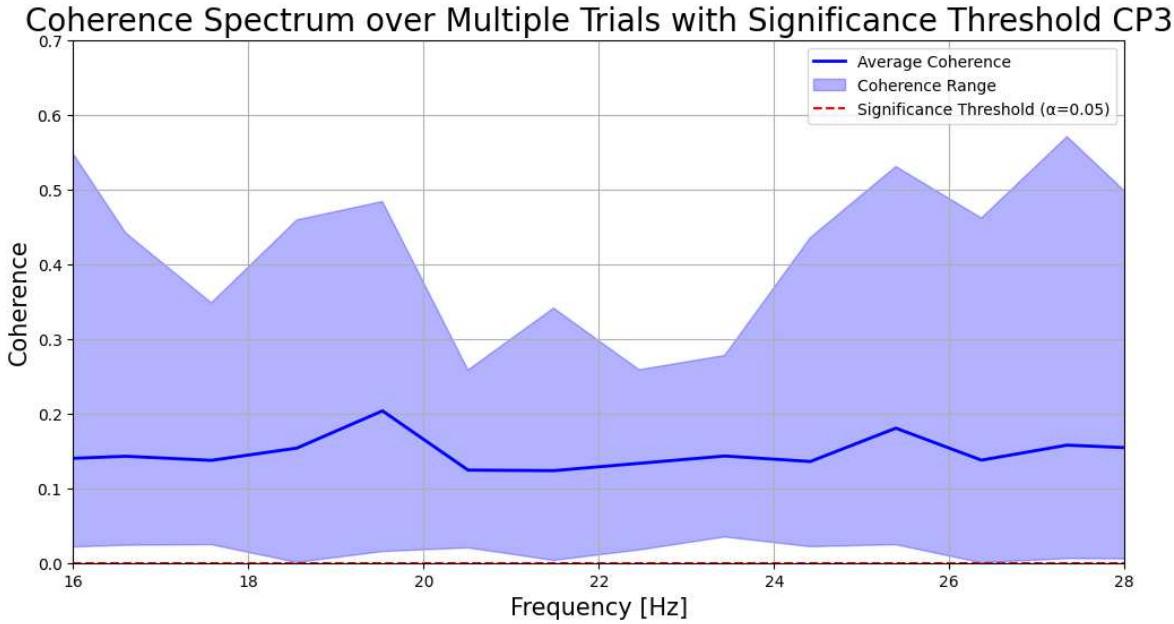


Figure 12. Cortico-muscular coherence peaks in the upper beta band region for CP3 electrode. As in Figure 11, this brain region controls the right hand, which is active; the corresponding activity is as anticipated. Alpha (α) represents the significance threshold of 0.05 above which coherence values are statistically significant.

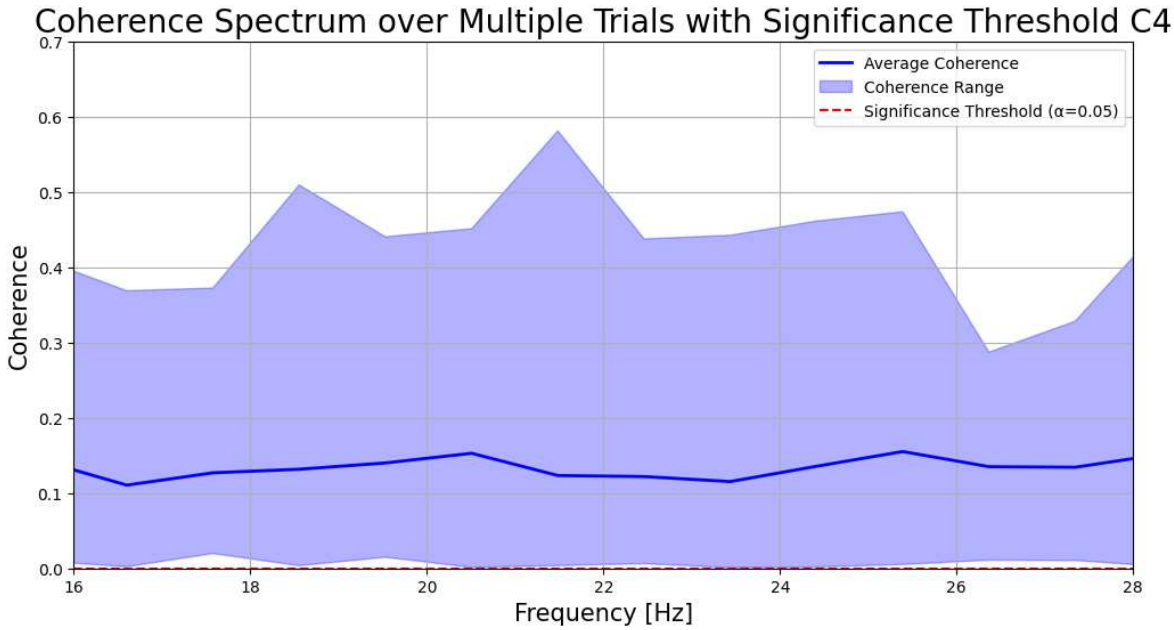


Figure 13. Lack of cortico-muscular coherence peaks in the upper beta band region for C4 electrode which is adjacent to the right motor cortex. Since this brain region controls the left hand, which is inactive, the corresponding lack of beta band peaks is as anticipated. Alpha (α) represents the significance threshold of 0.05 above which coherence values are statistically significant.

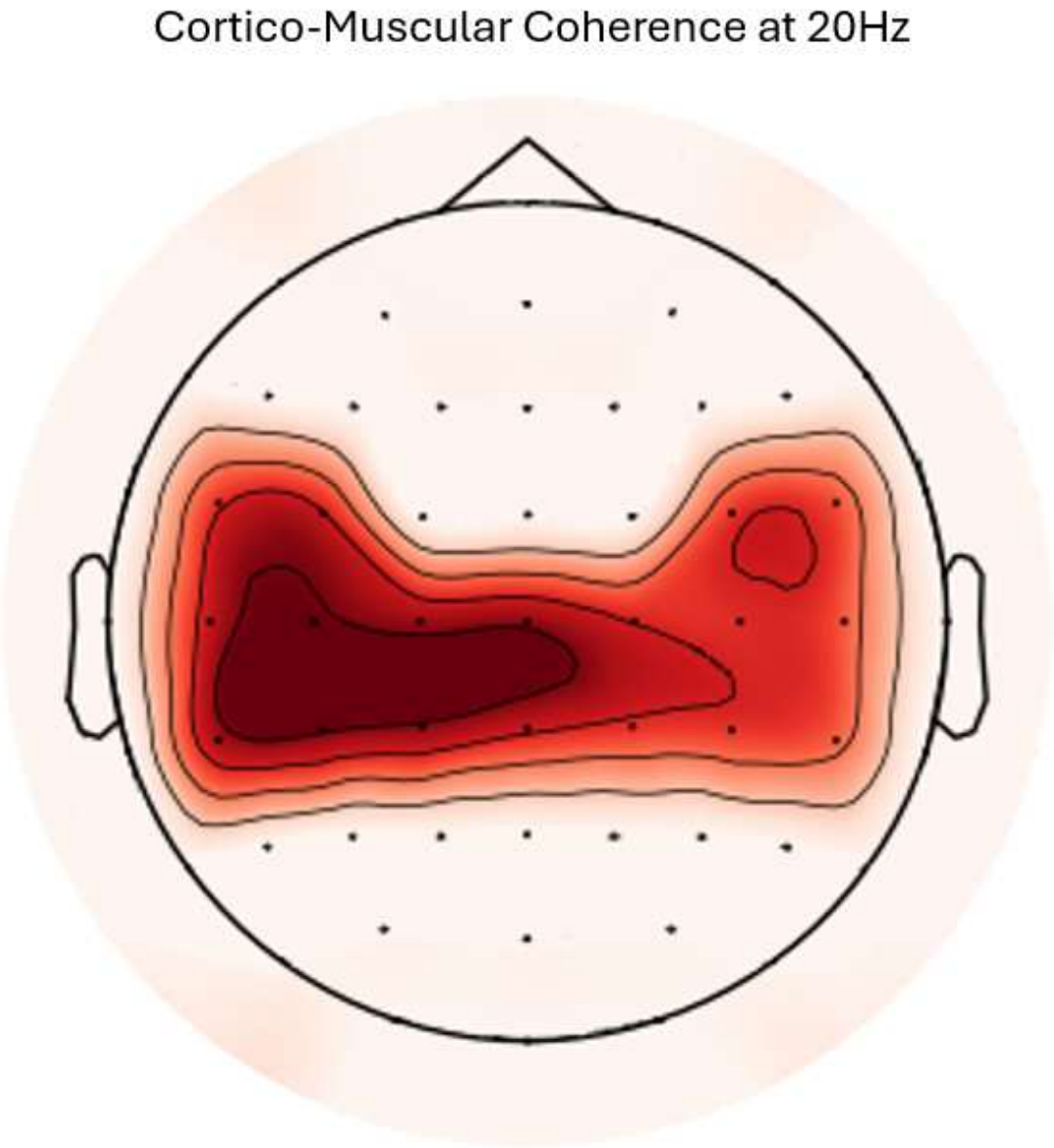


Figure 14. Scalp plot examining cortico-muscular coherence at 20Hz (the middle of the beta band). The result displays a higher value of cortico muscular coherence in the electrodes on the left side of the brain which is expected as the force contraction task was carried out with the right hand. The electrodes are shown as dots on the scalp plot with the active electrodes displayed within the boundaries of the red region and the unused electrodes displayed outside of this region. In total, 18 active electrodes where selected for placement due to their proximity to the motor and premotor cortices, which made them relevant to the study.

3.3. Real Time Motor Unit Decomposition

High density arrays provide high spatio-temporal sampling of EMG enabling the application of decomposition algorithms applied to the HD-EMG data such as motor unit decomposition for extracting the individual timings of motor unit action potentials (MUAPs) [20]. This allows for a more direct understanding and interfacing with the peripheral nervous system which may enable better peripheral nervous system-based brain computer interfaces such as those recently offered by Meta [2]. That being said, motor unit decomposition would also open up the potential for rehabilitation of neuromuscular disorders and stroke by means of motor unit activity based neurofeedback, especially if implemented in real time [21]. For implementation, classic blind source separation approaches were initially used to develop offline methods followed by online methods and more recently deep learning methods have been introduced. These approaches make use of developments in the field of AI to enable and create interaction between real (motor neurons) and artificial neurons [22][23].

The results shown in Figures 15, 16 and 17 are generated by means of a real-time motor unit (MU) tracking after application of the offline decomposition algorithm. The algorithm is first trained on a data set with a few seconds dedicated to each intended gesture. Then the realtime EMG data is fed into the algorithm containing the trained weights and a raster plot of motor unit spike locations is generated [22][23]. The generated output is a matrix of all detected motor units versus sample number with a 1 for a motor unit being detected and 0 otherwise. As for results, it should be noted that the decomposition may be incomplete and the algorithm could have potentially detected combined motor unit activities as one. The potential for this problem may be evidenced by similar motor unit activity across gestures and detected motor units.

As for the setup, the data was acquired from 128 channels in a manner similar to the one portrayed in Figure 6. Since the motor unit decomposition algorithm is two-part, two types of data were collected; training data and real time recording data. The training data was collected while performing a series of predetermined common hand gestures, such as wrist flexion, wrist extension, and making a fist, with all muscle contractions being isometric. The gestures were then maintained for 10-20s each in order to provide sufficient information for model parameter extraction using the classic independent component analysis (ICA) type blind source separation algorithm. The training data was then fed into an ICA type blind source separation algorithm to build a model with parameters based on the dynamics of motor unit activity in the given setup. Once trained, the second part of the algorithm (decomposition function), was setup with the obtained parameters, and data chunks with a length in the range of 1000-2000 samples were obtained and input into the decomposition function in real time, as detailed in 'System Description' and 'Online Decomposition' sections of [23] and [22], respectively. The function would then produce a list of spike times which was converted to a matrix

and displayed as an image as illustrated in Figures 15, 16, and 17.

Figure 15 shows a clear activation of motor units during index finger flexion and extension while Figure 16 examines the sensitivity to slight movements, in this case the pinky finger. Here, the EMG signals present lots of prominent individual spike-like neural activity often detected by the system. In addition, Figure 16 further indicates the detection of motor unit spikes where the activation pattern appears characteristic of continuous motor unit activity.

Finally, the system was tested while performing a hand grasp action in order to activate as many motor units as possible. As seen in Figure 17, there are very clear motor unit activation patterns with certain motor units being recruited and de-recruited at different times with some being activated before, during and towards the end of the main motion [24].

It should also be noted that further experiments would be required to substantiate that individual motor unit spikes were detected, filter out any possible false positives and separate any motor units that were combined as one. However, overall, the real-time motor unit decomposition experiments confirm the functionality of the $W^2Myolink$ as a practical and functional real-time 128 channel neural interface allowing for direct real-time feedback of motor unit activation.

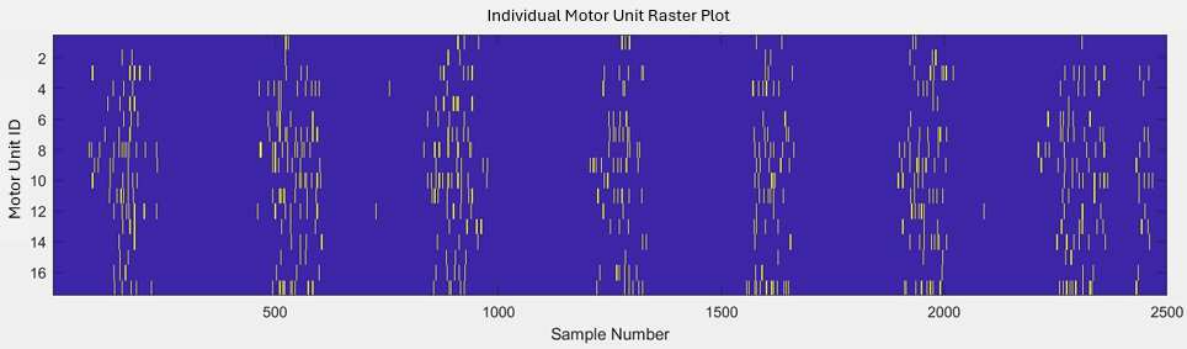


Figure 15. Result of detected motor unit activity from **wobbling the index finger**. Motor unit spikes displayed as a matrix of motor unit numbers against sample number with blue representing a value of zero (a lack of spikes) and yellow representing a value of one (the presence of a spike) in order to show firing times. It should be noted that although the firing patterns are regular and show recruitment and de recruitment at different times, the firing rates are significantly high which suggests a possibility that multiple motor units were grouped together.

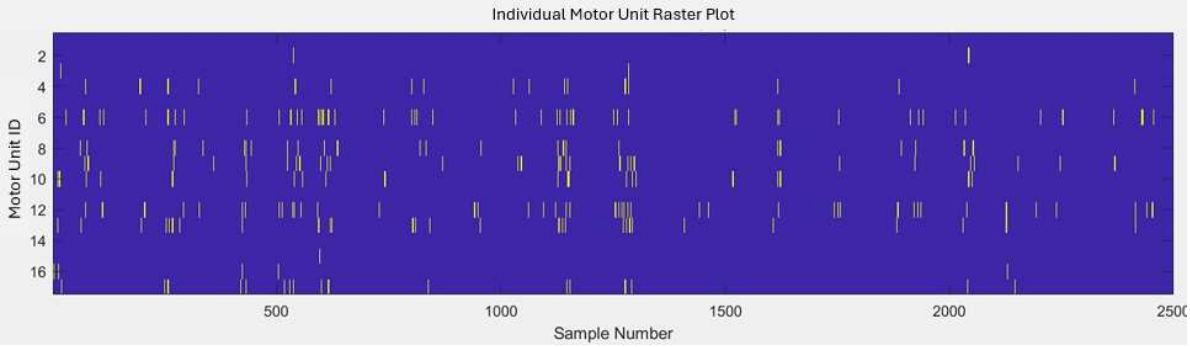


Figure 16. Result of detected motor unit activity when carrying out **small movements** (minimal flexions and extensions) **of the pinky finger**. Motor unit spikes displayed as a raster plot; a matrix of motor unit numbers against sample number, with blue representing a value of zero (a lack of spikes) and yellow representing a value of one (the presence of a spike) in order to show firing times. Although characterisitic firing patterns are visible, similar spike detection times across multiple motor units could indicate multiple motor unit activity combined into one.

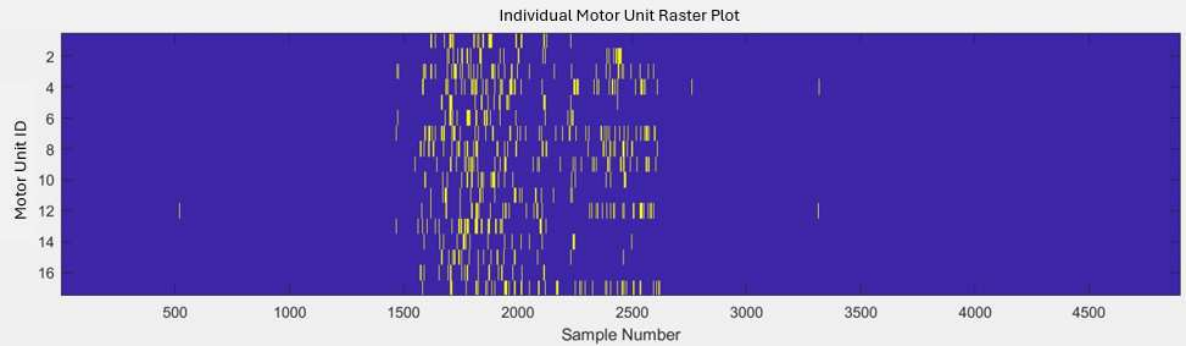


Figure 17. Result of detected motor unit activity when making a **tight fist**. Motor unit spikes displayed as a matrix of motor unit numbers against sample number with blue representing a value of zero (a lack of spikes) and yellow representing a value of one (the presence of a spike) in order to show firing times. Here we can see the firing patterns of each motor neuron which start and stop at different times, matching the motor neuron recruitment patterns which consist of motor units being recruited one after the other and at different times as exerted force is increased. With such rapid and larger scale movements, it maybe be important to evaluate the effect of motion artifacts, electrode detachment and shifting and other factors on the performance of the decomposition algorithm.

3.4. Playback of ALS data

Motivated by the need to exemplify the ability of the new device to capture with high-fidelity EMG data corresponding to different neuromuscular health state conditions, in this last customary experiment, EMG data corresponding to healthy subjects and subjects suffering from Amyotrophic Lateral Sclerosis (ALS), and other neuromuscular disorders, was played back into 64 channels of the instrument. The played back physiological data were sourced from 4 patients in [25]. The arbitrary waveform generator,

specifically the Keysight 33509B, was configured to play back data into the 64 channels of the device enabling a clean and consistent test signal to be input for examining the fidelity of the wireless data transmission. This controlled experiment, thus, allows for the evaluation of the transmission fidelity of the device.

Figure 18 (**top**) illustrates the played-back EMG data from a healthy subject while Figure 18 (**bottom**) illustrates the same data after they have been transmitted and received wirelessly. In Fig. 18 (**top**) the average of all 64 channels is also depicted. The NMRSE error between the original played-back data and the wireless data amounts to 0.0873.

Similarly, Figures 18, 19 and 21 illustrate played-back EMG data corresponding to myopathy, neuropathy and ALS respectively. The wirelessly transmitted and received data from 64 channels in each pathology case are shown at the bottom of Figures 18, 19 and 21; the average of all 64 channels is also illustrated in each one of the wireless data figures. The NMRSE error between the original played back data and the wireless data was 0.0766, 0.0361 and 0.1814 for the case of myopathy, neuropathy and ALS respectively.

Based on the NMRSE values reported, one can conclude that the new device is indeed capable of capturing and wirelessly transmitting different muscle pathologies with satisfactory fidelity.

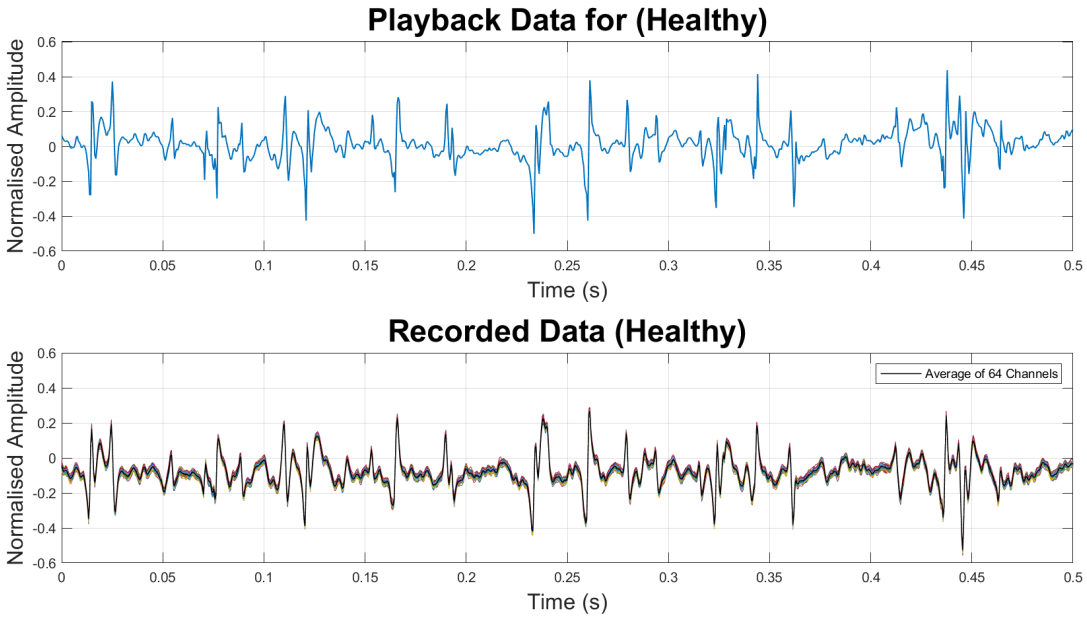


Figure 18. **Top**: Played back EMG data from a healthy subject. **Bottom**: Concurrently and wirelessly transmitted and received data in **Top** from 64 channels of the device. The NMRSE (normalised root mean square error) value between the original data in **Top** and the average value of the 64 channels in **Bottom** is 0.0873.

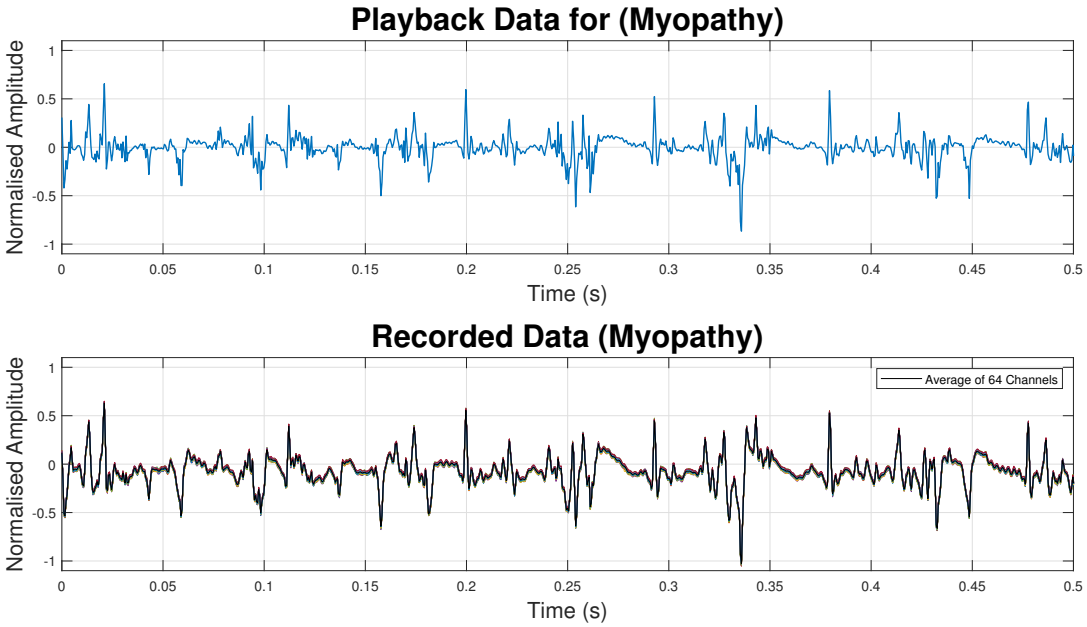


Figure 19. **Top**: Played back EMG data from a subject with myopathy. **Bottom**: Concurrently and wirelessly transmitted and received data in **Top** from 64 channels of the device. The NMRSE (normalised root mean square error) value between the original data in **Top** and the average value of the 64 channels in **Bottom** is 0.0766.

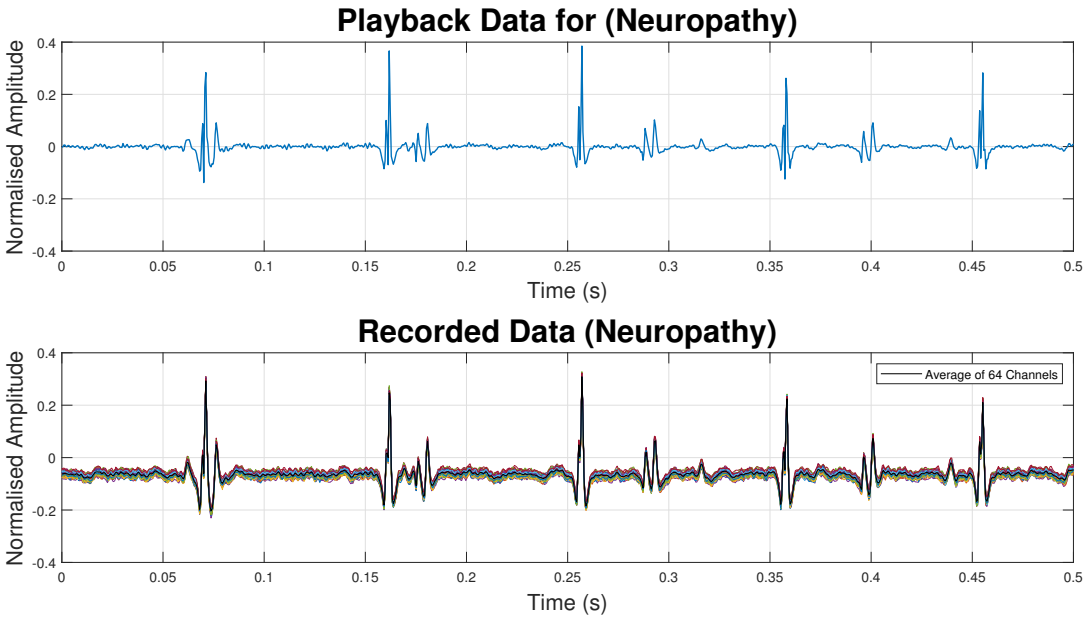


Figure 20. Top: Played back EMG data from a subject with neuropathy. **Bottom**: Concurrently and wirelessly transmitted and received data in **Top** from 64 channels of the device. The NMRSE (normalised root mean square error) value between the original data in **Top** and the average value of the 64 channels in **Bottom** is 0.0361.

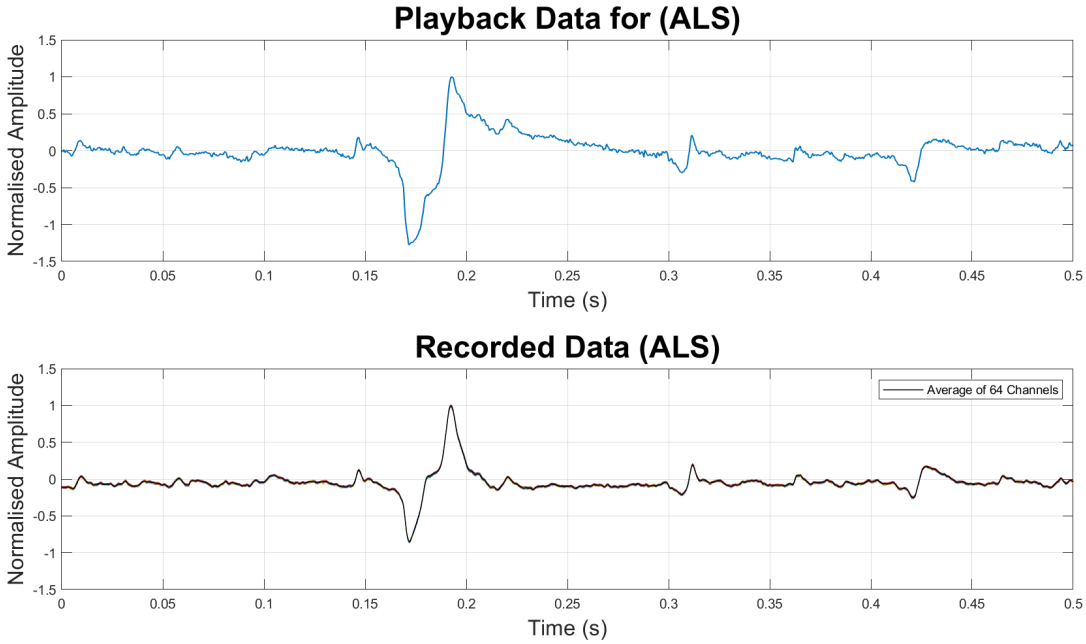


Figure 21. Top: Played back EMG data from a subject with Amyotrophic Lateral Sclerosis (ALS). **Bottom**: Concurrently and wirelessly transmitted and received data in **Top** from 64 channels of the device. The NMRSE (normalised root mean square error) value between the original data in **Top** and the average value of the 64 channels in **Bottom** is 0.1814.

4. Complex Experiments

These experiments aim at the full deployment of the device, highlighting how they would be difficult to conduct or even not possible without wireless capabilities and how it would be difficult to acquire such data with such detail using existing technologies.

4.1. Human Robot Interaction - ISYBOT

One of the main research fields of HD-EMG is human robot interaction [26] . This experiment aims to investigate that interaction by means of a setup involving an interactive game with a treadmill, a 180 degrees screen, multiple infrared cameras and the possibility to use two ISYBOT robotic arms for support and haptic feedback during the game; the details of the full setup are shown in Figure 22 which illustrates each of the aforementioned parts assembled together in one room.

The chosen game involved a subject walking down a road through the countryside on a varied terrain and swatting bird and butterflies, flying at the walker, out of the way using either hand gestures or robot assisted movements while the $W^2Myolink$ recorded the EMG signals. This immerses the user in the environment allowing for natural motion our $W^2Myolink$ device can measure in an unintrusive manner.

Such a game comprises a complex environment in which the deployment of a wired device would not be ideal (or even possible) due to a crowded setup and a multitude of moving parts; but still an environment in which the $W^2Myolink$ can fill its niche and allow for dynamic wireless recordings and synchronisation with the camera recordings.

Figure 23 captures a scene of gesture based game play without the guidance of the ISYBOT seen in Fig. 22 when preparing to swat a butterfly, swatting the butterfly and re-establishing original hand position with two 64 channel electrode grids placed on the top and bottom side of the right forearm. The figure illustrates three frames in red, green and blue corresponding to these three events and portrays and describes the changes in muscle activity before, after and between these frames through visual and quantitative methods; more specifically, the channel RMS value and its average in each frame defined time segment. The average RMS values are 64.3μV before Frame 1, 97.2μV between Frame 1 and 2, 80.4μV between Frame 2 and 3, and 72.7μV after Frame 3 with expected increases in between Frame 1 and Frame 3 due to the change in motion. It is also interesting to note that EMG activity before Frame 1 is normally constant and high in amplitude with significant RMS values due to the need to constantly support the arms in the air and only changes when there is a change in direction of motion due to the need to apply force. The EMG activity and RMS value also decrease to near zero around Frame 1 when the arm is just about to fall back down from a higher position being consistent in the short-lived free fall condition of the arm.

Figure 24 corresponds to results involving the ISYBOT robotic arms and the support they can offer. Observe that the recorded EMG activity remains almost constant because of the constant support of the robot but also the need to maintain a steady grasp of the ISYBOT robot hand interface tip (see Fig. 22, label 3). This steady grasp is essential for interaction with the robot in order to move with the ISYBOT arm with ease and stabilise haptic feedback that it provides. As for quantitive results, we obtain an average RMS value of 55.2μV before Frame 1, 57.6μV between Frame 1 and Frame 2, 75.8 between Frame 2 and Frame 3, and 75.0μV after Frame 3. While there is only a mild increase from the RMS value of 55.2μV to 57.6μV indicative of gently pushing the ISYBOT arm into position to swat the bird, the increase to 75.8μV and 75.0μV indicates the extra force necessary to quickly pull the robot arm back towards the subject and stabilise haptic feedback upon contact with the bird. In addition, all average RMS values are, in general lower than in Figure 23 indicating contributing support from the robotic arms.

This study confirms the practicality and the ability of our $W^2Myolink$ to conveniently collect 128 channels of high density sEMG recording even at complex experimental setups which involve human motion both with and without human-robot interaction, a fact that adds progressively to the field.

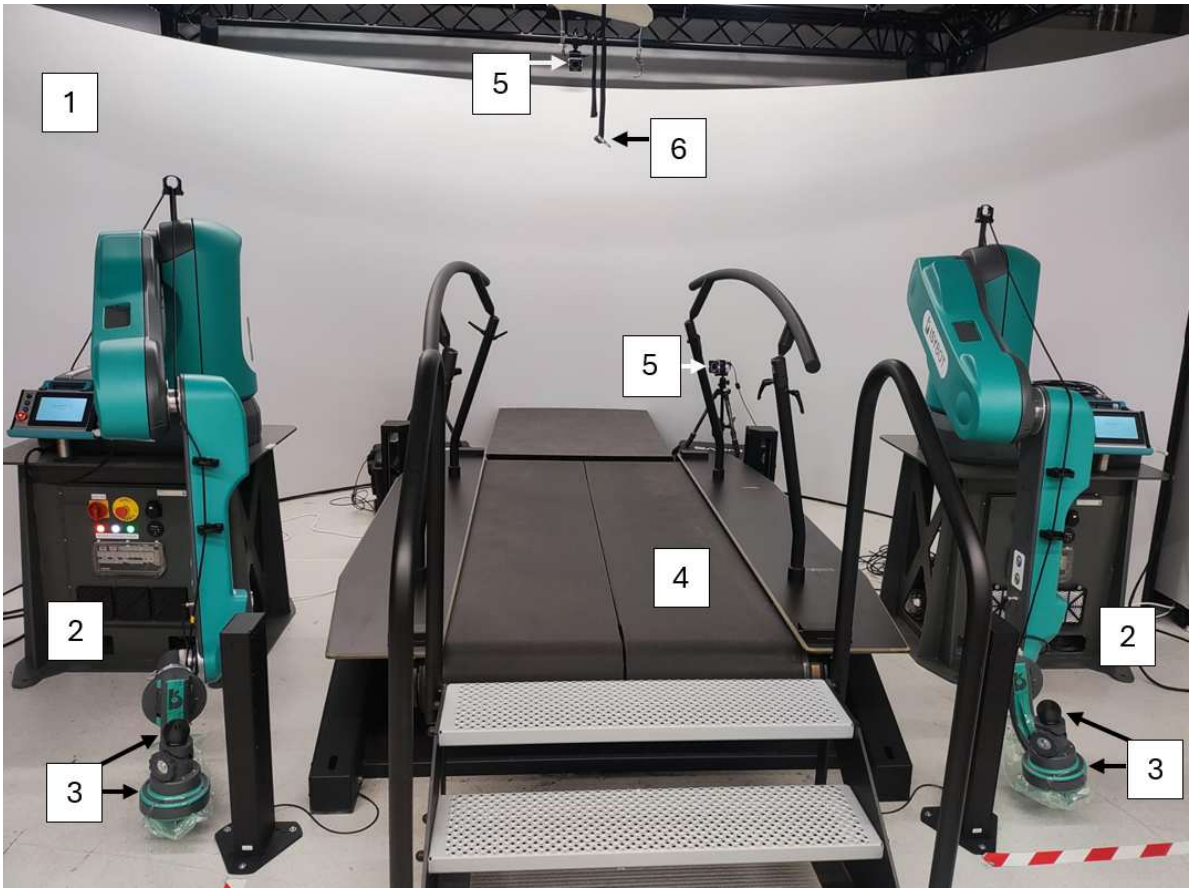


Figure 22. Full setup of ISYBOT experiment. 1 180 degree screen for displaying the interactive game, 2 ISYBOT main body, 3 Terminal end of ISYBOT arm interface (subject grabs onto the black sphere), 4 Adjustable incline treadmill, 5 Near infrared cameras (night vision), 6 Subject safety harness attachment clip.

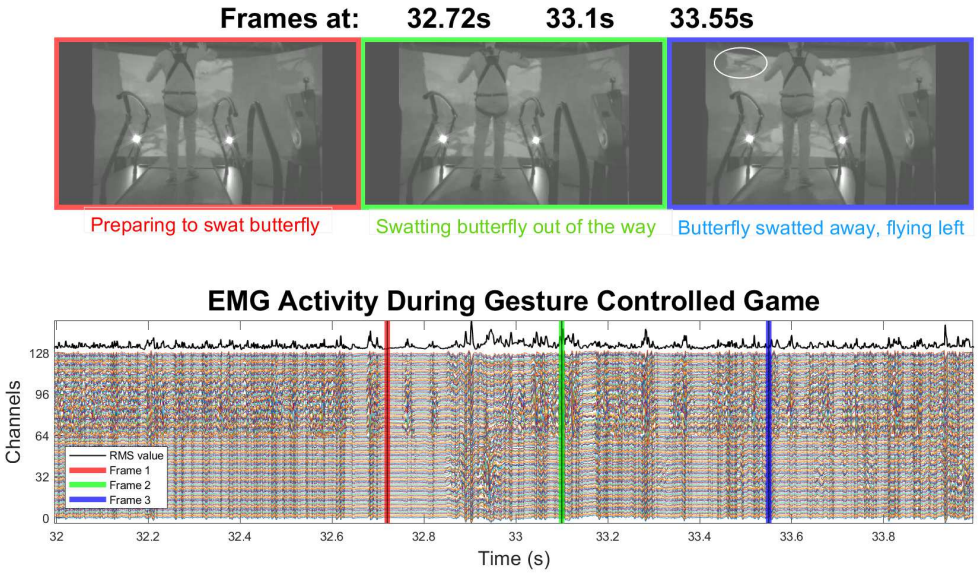


Figure 23. EMG recordings from 128 channels during a gesture controlled game without ISYBOT assistance; the subject plays a game involving swatting butterflies and birds out of the way. The bottom graph indicates EMG channels and the average RMS value and the red, green and blue lines correspond to the times at which 3 frames (labelled frame 1: red, frame 2: green, and frame 3: blue) were taken, visible in an image frame of the same colours in the top image. The continuous EMG activity, as indicated indicated in the EMG channels and RMS values, seen before frame 1 occurs due to maintaining the hand in a stable position in front of the body in preparation to swat the butterfly, with a lower RMS value of 64.3μV. Between frame 1 and frame 2 the subject directs their hand to swat the butterfly and between frame 2 and frame 3 the subject successfully swats the butterfly (visible in white oval in the frame 3 image) and brings their hand back to the central position. Due to the change in hand position and movement being the greatest here (we can observe large changes in the activity of the EMG channels and significant increases in channel RMS value with multiple peaks visible), the average of the RMS value rises to 97.2μV and 80.4μV respectively. Finally, in frame 3, the subject attempts to get their hand in a stable position in preparation for swatting the next bird or butterfly to come, reflected in fewer changes in the EMG activity and the channel RMS value, with its average falling to 72.7μV.

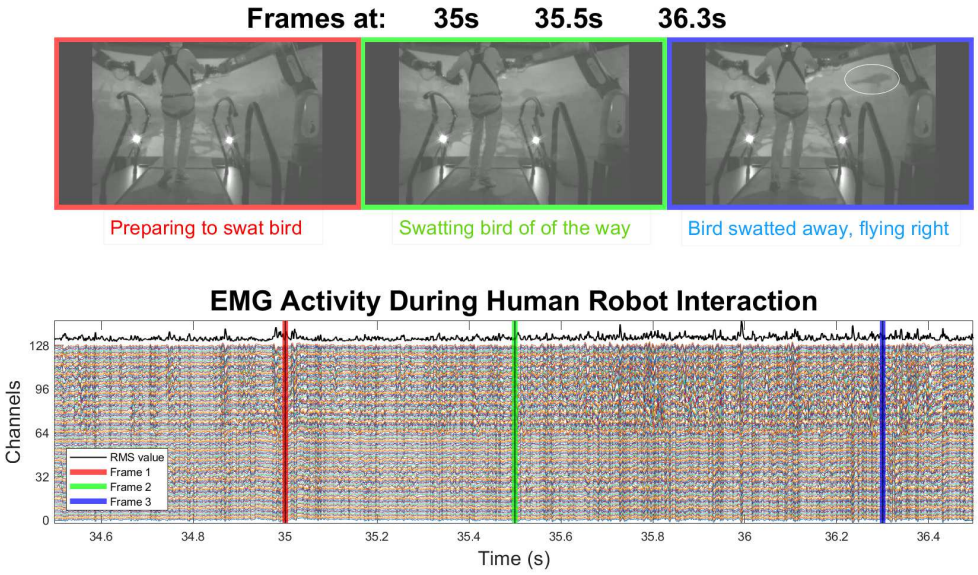


Figure 24. EMG recordings from 128 channels during a gesture controlled game with ISYBOT assistance; the subject plays a game involving swatting butterflies and birds out of the way. The bottom graph indicates EMG channels and the channel RMS value and the red, green and blue lines correspond to the times at which 3 frames (labelled frame 1: red, frame 2: green, and frame 3: blue) were taken, visible in an image frame of the same colours in the top image. Due to the support of the robot arms, the activity does not fluctuate significantly although it remains significant due to the need to maintain a constant grip on the robot arm gripable interface. The EMG activity ,as indicated in the EMG channels and RMS values, seen before frame 1 is significantly low (average RMS value of 55.2μV) as the subject prepares to swat the bird, relaxing their hand in preparation for a stronger grip. Between frame 1 and frame 2 the subject directs their hand to swat the bird seen by the changing in position visible in the image corresponding to Frame 2, despite this the average RMS value remains low at 57.6μV. Between frame 2 and frame 3 the subject successfully swats the bird (visible in white oval in the frame 3 image) and brings their hand back to the central position; the EMG activity and channel RMS values here are increased (average RMS value increases to 75.8μV) as the subject absorbs the haptic feedback from the robot arms and pulls the robot arms back towards themselves. Finally, in Frame 3, the subject successfully swats the bird away (as shown in the white oval) and proceeds to get their hand in a stable position in preparation for swatting the next bird or butterfly to come. The average RMS value remains high at 75.0μV.

4.2. Experimentation with Exoskeleton in the Operating Theatre

Novel surgical techniques, especially those involving a large gamut of sophisticated equipment and robots is a fast growing field [27]. One aspect of surgery that is often overlooked is the monitoring of performance during surgery: due to the fact that surgeons are often required to perform precise movements for extended periods of time, indications for the surgeon's muscle fatigue and concentration are significant factors to consider.

In this experiment, we set out to monitor the surgeon's muscle activity and fatigue in the case when an exoskeleton supports or does not support the surgeon's upper arms. Given the limited space available in the operating theatre, particularly for this type of experiment which already involves a bulky exoskeleton, the deployment of the new wireless device is particularly practical; the deployment of a wired device with the same number of channels in the specific operating theatre would be challenging.

The electrode grids used were placed on the back of the surgeon and were of two types as shown in Figs. 25 and 26. Due to being one continuous flexible electrode (which differs from the electrodes used in other experiments in this paper), data recorded by means of the continuous electrode of Fig. 25 are chosen for analysis. Figures 27 and 28 show the front and rear view of the practical setup with the exoskeleton. As shown in Figure 27; the exoskeleton is equipped with arm bands that are placed under the arms of the surgeon for support. On the other hand, Figure 28, shows the rear side of the setup and how the $W^2Myolink$ is secured to the exoskeleton along with the support spring mechanism visible on the back.

The Ottobock IX Shoulder exoskeleton shifts load from the arms to the lower back thereby moving the neutral position of the arms from hanging down to resting in front of the torso at a 60-90 degree angle from the legs relieving the need to keep muscles contracted in order to keep the arms "up and in front" during surgery.

During the experiment, four different test conditions are considered: i) recording of baseline EMG activity, ii) maximum muscle exertion with exoskeleton in the OFF position. iii) exoskeleton ON (the exoskeleton is worn) iv) exoskeleton OFF (the exoskeleton is still worn but the arm support bands are pushed up, removing any supportive action). Figure 29 illustrates the exoskeleton in the OFF position with the arm support cuffs pushed up.

Four different types of surgery were performed each one involving the four aforementioned test conditions. The four surgeries performed were tympanoplasty, sinus surgery, thyroid cancer removal and nasal polyp removal. Figure 30 illustrates in bar chart format the RMS activity for each one of the four surgeries and for each one of the testing

conditions. The results clearly demonstrate that, as expected, the test conditions involving the exoskeleton ON are contained between the baseline and the maximum exertion, RMS value of activity and RMS values are lower as when compared to the "exoskeleton OFF" test condition. This was seen in all four surgeries all of which required different sets of manual skills.

Figure 31 combines the recordings for all four testing conditions for the tympanoplasty surgery; one observes a clear increase in muscle activity across all 128 channels when the exoskeleton is OFF vs. the case when the exoskeleton is ON. The changes in activity are further examined in Figure 32 which reveals clear double-sided diagonal bands of muscle activity reflecting the distinct orientations of the shoulder muscles. Observe that during the "maximum exertion" test, both sides of the muscles are active to a similar degree. Furthermore, the exoskeleton OFF condition corresponds to higher muscles activity when compared against the exoskeleton ON condition; in both cases higher muscle activity is recorded for the more active right arm than for the less active left arm. Figure 33 captures metrics related to the complexity of the recorded signals and the density of information recorded: a correlation matrix is produced for all four testing conditions for the tympanoplasty surgery; it can be observed that most electrode signals of the 6x21 grid array have correlations of limited strength which suggests a high degree of independence as far as the information recorded by each channel/electrode is concerned.

Finally, Figure 34 depicts the metrics of Lempel Ziv Complexity (LZC) and entropy for each one of the four testing conditions and for the case of endoscopic sinus surgery. Although commonly used for investigating brain states ([28]) and being potentially different across surgeries, one observes an increase in LZC but a decrease in entropy for the "maximum exertion" testing condition compared to the rest condition which can be interpreted as the rest condition being characterised by more random activity, and hence more entropy, whereas the "maximum exertion" condition as being characterised by less random but more complex activity. Moreover, both LZC and entropy drop when the exoskeleton is in the OFF condition which suggests that activity becomes less complex and less random.

To conclude, the deployment of the device in a variety of four different surgeries with a large gamut of analysis and techniques applied to analyse and portray the quality of EMG data and information obtained. As shown in Figures 30, 31 and 32 through multiple data analysis methods, the analysis has successfully demonstrated that the exoskeleton, when ON, does decrease the amplitude of muscle activity, thereby decreasing the muscle fatigue during surgery. In addition, Figures 32, 33 and 34 demonstrate the complexity of the data acquired conveying the successful wireless acquisition of 128 HD-EMG channels in real-time live surgery. As such, this complex experiment has showcased a successful study of experimentation with the exoskeleton in the operating theatre, investigating muscle fatigue and the complex neuromuscular

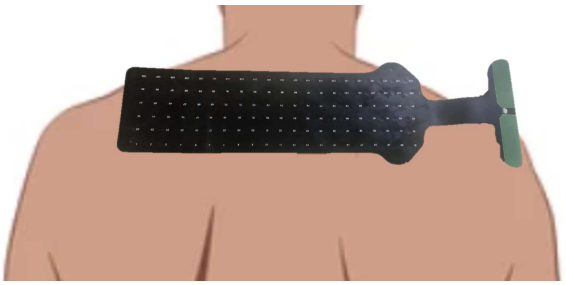


Figure 25. Setup 1: Placement of custom-made 128 channel electrode across the back of the surgeon (bear in mind Fig. 3).



Figure 26. Setup 2: Placement of two 64 channel standard bioelettronica electrodes on the trapezoid muscles of the surgeon (bear in mind Fig. 3).

dynamics of performance in the operating theatre.



Figure 27. Front view before surgery: the Ottobock exoskeleton in the ON position; note the exoskeleton arm supports labelled in the image above that keep the exoskeleton in place and provide support to the arms.



Figure 28. Rear view before surgery: the Ottobock exoskeleton and the W^2 Myolink are set-up and ready to go.

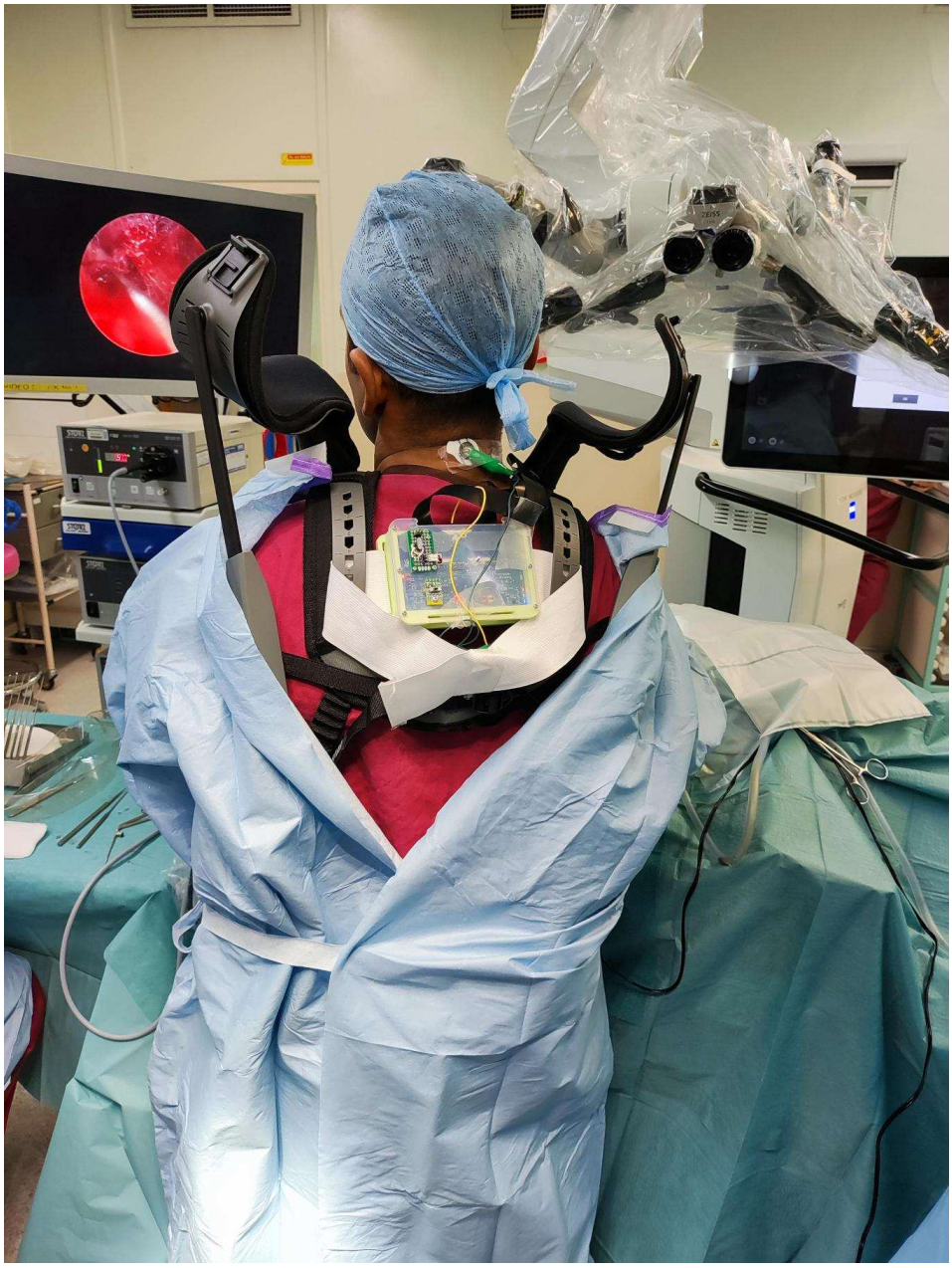


Figure 29. Rear view during surgery: the exoskeleton is in the OFF position: the semi circular support cuffs can be seen off while the exoskeleton remains on the surgeon for practical purposes and as a control measure for weight.

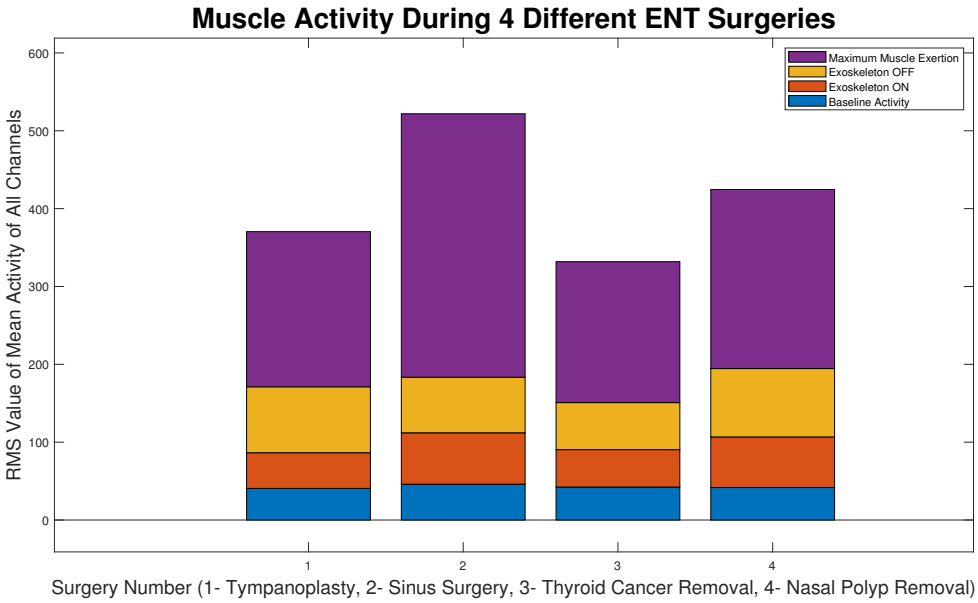


Figure 30. Graph illustrating the RMS value of the mean muscle activity during four different types of surgery; namely tympanoplasty, sinus surgery, thyroid cancer removal and nasal polyp removal, with and without the exoskeleton, compared against "baseline" and "maximum muscle exertion" conditions.

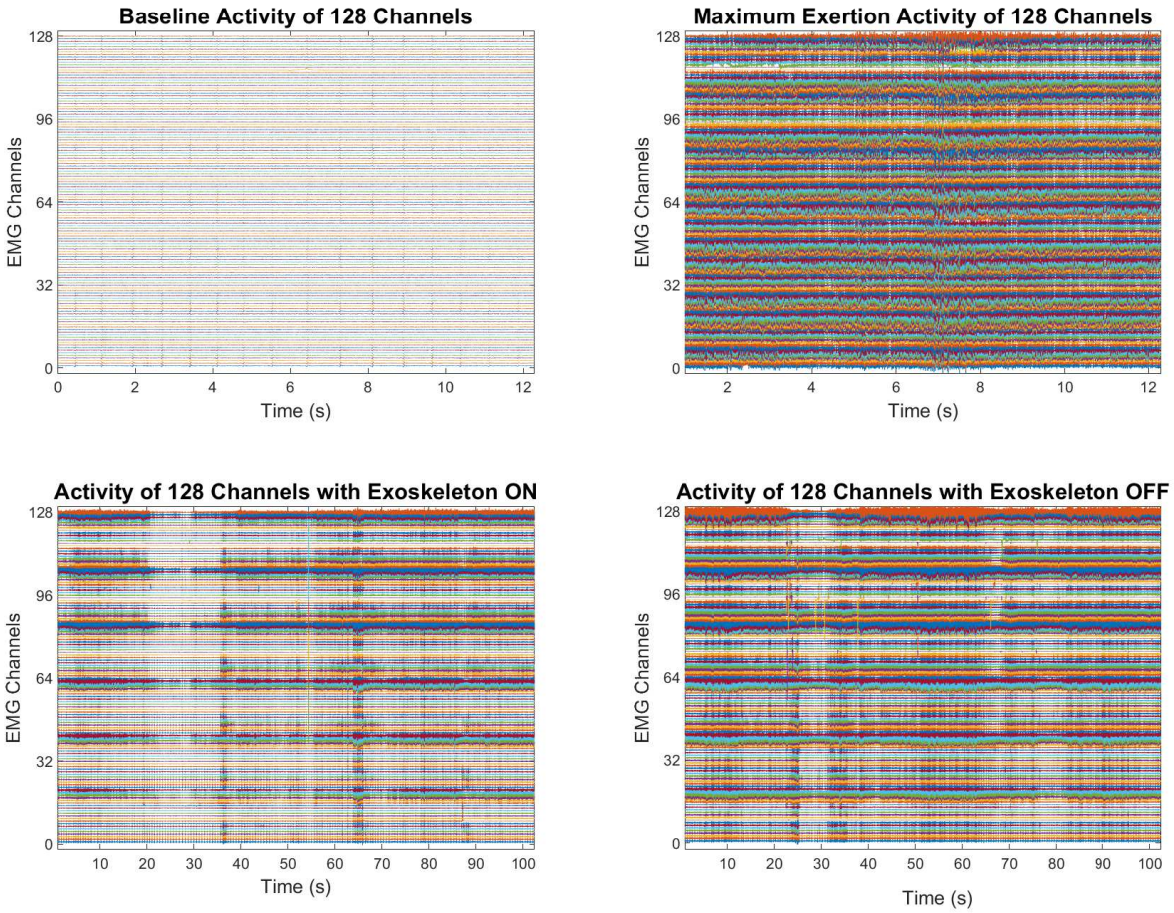


Figure 31. Muscle activity for all 128 channels displayed in time for all four conditions for the tympanoplasty surgery. Note the clear increase in muscle activation for the case when the exoskeleton is OFF vs ON. (**Top Left**) The baseline activity of the full set of 128 channels; there appears to only be minimal background activity. The repetitive background signal could be attributed to the electrocardiogram (ECG) due its frequency of around 75-80 occurrences per minute. (**Top Right**) Activity of all channels at maximum exertion; sparing a few channels in the top section of the plot, there is generally equal and high amplitude EMG activity, as anticipated. (**Bottom Left**) and (**Bottom Right**): activity with the exoskeleton ON and OFF respectively, with a distinctly higher amplitude for the latter. Note that the time range is larger for the bottom panels (100s) instead of 12 seconds for the two top panels to illustrate that the amplitude levels are consistent for over a minute of surgery.

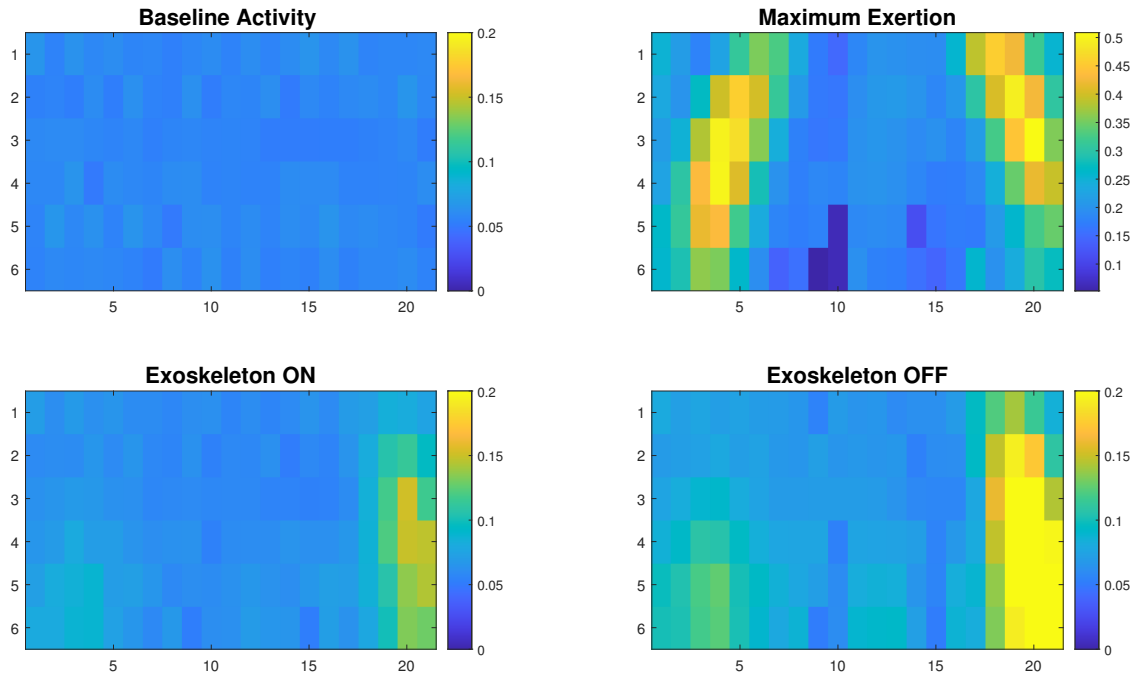


Figure 32. Electrode array maps showing the EMG activity power for each electrode in the 6*21 grid for all four testing conditions for the tympanoplasty surgery with the numbers on the colour bar representing the mean absolute signal values in millivolts. (**Top Left**) For the rest condition, as anticipated, minimal activity is visible in the plot. (**Top Right**) Two distinct bands are visible here representing the activity coming from the upper back muscles; note the bands are of different shape when compared to with the Exoskeleton ON and OFF conditions suggesting a distinct set of muscles being activated. Note that the dark blue squares represent disconnected or badly contacting channels and the color bar ranges from 0 to 0.5 to enable the visibility of the higher amplitude signals. (**Bottom Left**) and (**Bottom Right**): Similar patterns of activity are visible with two distinct bands; the right band presenting higher activity than the left band corresponding to a more active right arm. Comparing (**Bottom Right**) with (**Bottom Left**) clearly illustrates a substantial increase in activity with the exoskeleton OFF than with the exoskeleton ON; however, the approximate shape of the activity remains the same for both maps indicating that the exoskeleton has successfully reduced the muscle activity and hence the muscle fatigue the exoskeleton ON case.

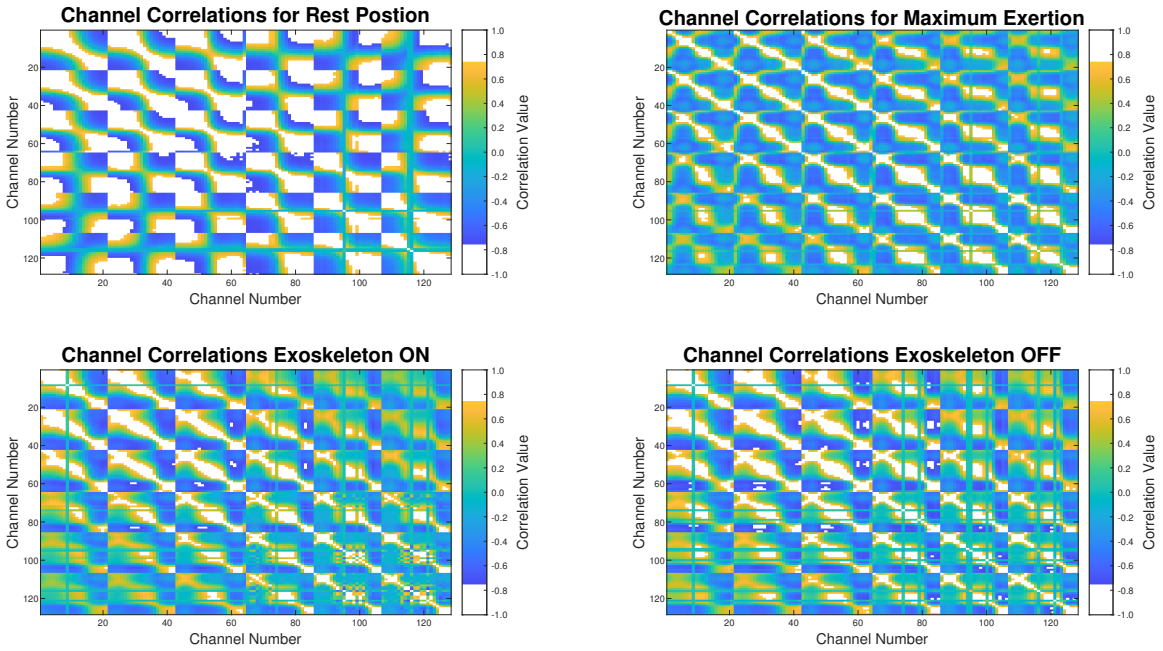


Figure 33. Correlation matrices for all channels, for each of the four conditions for tympanoplasty surgery. Strong correlation values (above 0.75 and below -0.75) have been whited out. The plots reveal that most electrodes have correlations with limited strength, demonstrating the independence of each channel and, in general, the unique information collected from each electrode of the 6x21 array. The rest condition (**Top Left**) contains the most white areas which illustrate high correlations between channels whereas the maximum exertion condition (**Top Right**) and live surgery with the Exoskeleton ON (**Bottom Left**) and OFF (**Bottom Right**) show more areas with intermediate colours (light blue, cyan and green) illustrating a range of correlations and suggesting a complex set of distinct signals from each channel. Note that the lines that do not fit the pattern are caused by disconnected channels.

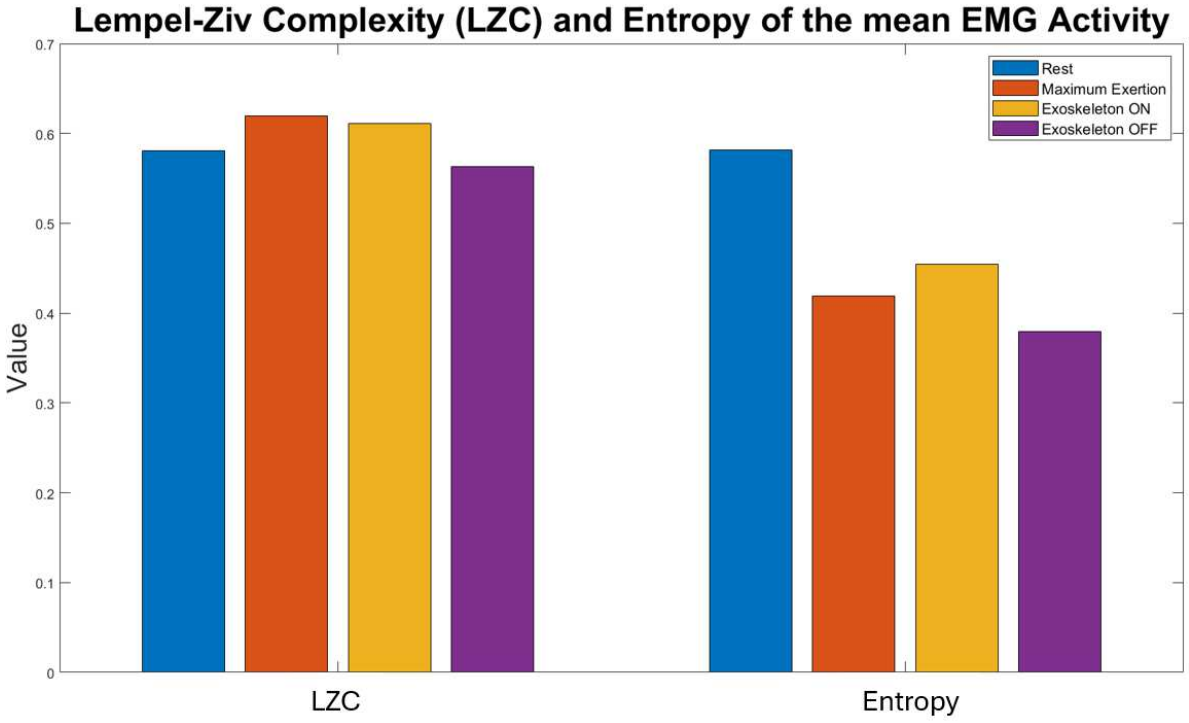


Figure 34. The application of Lempel Ziv Complexity metric and Context Tree Weighting (CTW) Entropy during endoscopic sinus surgery show clear results: both complexity and entropy are higher with the exoskeleton ON than OFF possibly suggesting more controlled and composite movements when the exoskeleton is ON as more of the activity corresponds to finer movements of back muscles. There is also a drop in entropy but an increase for LZC for the 'maximum exertion' condition compared to rest, suggesting more structured but less random activity which is expected.

4.3. Psychedelic Experience Monitoring

Research in psychedelics and altered states of consciousness has been a rapidly expanding field in the past few years and has revealed substantial evidence for the use of psychedelics in controlled and serious settings for treating various mental disorders, such as depression, addiction and obsessive compulsive disorder (OCD), as well as for their use as tools to investigate consciousness and the brain [29].

However, most studies in psychedelic research focus on the brain and make use of subjective experience questionaries, rarely focusing on the peripheral nervous system [29]. This general lack of monitoring and investigation of the peripheral nervous system in brain studies is somewhat surprising given that body signals could also be considered neural correlates as peripheral nervous system is strictly speaking an extension of the central nervous system. The peripheral nervous system frequently presents important markers of various biological and diseased states; such as in Parkinson's related tremor, in states of stress and relaxation, or when under the influence of a psychoactive substance such as jitters and high heart rate from caffeine or unstable gait from alcohol.

Regarding psychedelics, there has, however, been one study entitled 'The Entropic Heart Paper' ([30]) which investigated reading brain entropy through analysis of heart rate entropy (and other metrics) under dimethyltryptamine (DMT), psilocybin, lysergic acid diethylamide (LSD) and ketamine and demonstrated significant correlations between heart and brain entropy. The paper concludes saying that the ability to monitor altered states of consciousness via heart signals alone opens new opportunities for practical applications and could be '*leveraged to build reliable predictors of specific aspects of experiences under altered states of consciousness*'.

As such, being inspired by [30] and the results from section 3.2 [18][19], the use of EMG to monitor the psychedelic experience represents an interesting application of the device. Not only can more information be gathered from the muscles than just the heart beats, the acquisition of HD-EMG signals enables the study of information flow through the neuromusclar system.

Thus, this experiment aspires to contribute to both the field of psychedelic research in developing novel methods for monitoring the psychedelic state through the peripheral nervous system, but also leverages psychedelics as tools to study the flow of information through the neuromuscular system which could contribute to better peripheral brain computer interfaces.

Electromyography signals were recorded as part of the pilot testing phase of the main trial of the DIPP research project at UNITy UCL where consenting subjects were given 25mg of psilocybin, and recordings were collected at baseline (before dosing), 90 min-

utes past dosing (the peak of the trip) and 150 minutes past dosing (near the half life of psilocybin). The device was set up on the upper arm as shown in Figure 35 with 5x13 Bioelettronica electrode grids (see Fig. 3). That location allowed for more flexible setup and free movement as well as better recording quality due to less body hair.

The collected data was then analysed by chopping it into segments of 10000 samples (approximately 5 seconds) and running entropy, Lempel Ziv Complexity (LZC) and frequency domain analysis on each segment. This makes data processing more efficient and allows for rejection of corrupted sections.

Figure 36 illustrates all clean traces for each condition with the average value being plotted in black. From the experimental graphs, it is deduced that there are peaks of EMG activity in the 8 to 24Hz frequency range after dosing that are not visible in the baseline condition. These peaks occur consistently across segments and are predominantly in the range of the beta band of brain activity. As such, this plot suggests the ability to detect neural correlates of the psychedelic state in EMG activity [18][19].

Table 2 lists the average LZC and CTW entropy values across segments and along with an additional metric termed Multiscale Entropy from EntropyHub [31]. For the Peak (P) case, LZC, entropy and multiscale entropy all appear to increase compared to the Baseline (B) case. Considering the multiscale entropy values, they appear to indicate that large scales are necessary to detect entropy changes effectively.

Given that psilocybin increases the entropy and complexity of brain activity [32], observing such an increase in EMG activity suggests successfully detecting the signatures of brain changes caused by psilocybin in the peripheral nervous system. In addition all increases in the metrics were found to be statisitically significant based on a t-test further solidifying the validity of the results. On the other hand, admittedly, there are limitations to this study, given the lack of synchronised EEG recording necessary to fully substantiate the origin of the EMG signal in the brain, limitation to one person and a lack of different positions when recording; all of which could relate to hidden variables affecting the experiment.

To conclude, it can be argued that this pilot study represents a successful attempt at monitoring the psychedelic state through the peripheral nervous system with statistically significant changes in entropy, complexity and power band activity. Even though the study is limited by sample size, it demonstrates a novel and interesting application of our $W^2Myolink$ to psychedelic and consciousness research as well as the potential of using the peripheral nervous system to monitor psychological state and to improve the reading of brain changes in muscles for better brain computer interfaces.



Figure 35. The $W^2Myolink$ placed on the upper arm. The electrodes are placed on the upper arm due to less hair being present there than on the forearm.

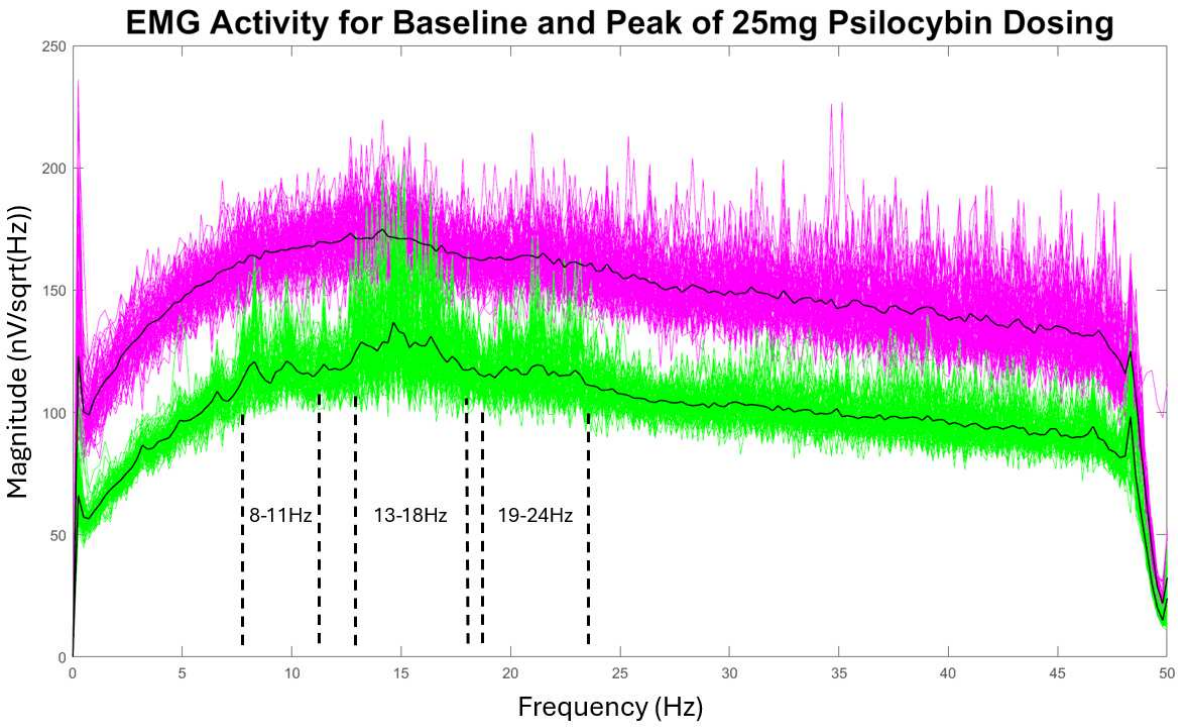


Figure 36. Comparison of EMG activity before (magenta) and at the peak of the effect of psilocybin (green) with their respective means depicted by a thicker black line. Compared to the baseline case increases in activity are observed in the 8-11, 13-18 and 19-24 Hz ranges. These frequency bands correspond broadly to the alpha and beta band of EEG (Corticomuscular Coherence [17]) which suggests a possibility of detecting psychedelic drug induced brain changes in muscle activity.

Table 2. Comparison of different metrics (LZC, CTW Entropy and Multiscale Entropy) to evaluate EMG activity under psilocybin.

Table	Baseline (B)	Peak (P)	% P/B
Lempel Ziv Complexity Subject 1	0.8359	0.8571	1.0254
CTWEntropy Subject 1	0.7986	0.8284	1.0372
Multi Scale Entropy Large Scale Subject 1	1.8138	1.8992	1.0471
Multi Scale Entropy Medium Scale Subject 1	1.9759	1.9988	1.0116
Multi Scale Entropy Small Scale Subject 1	1.8804	1.8894	1.0048

5. Discussion

This paper has introduced the Wireless Wearable (W^2) Myolink, a new micro-instrument capable of low-noise, high-performance recording and wirelessly transmitting (WiFi) 128 channels of high-density surface EMG signals. The range of multidisciplinary experiments conducted and presented in this paper confirm the practicality of the $W^2Myolink$ when deployed, along with its ability to indeed collect high-quality EMG data.

Both customary and more complex experiments from a variety of disciplines have exemplified the usefulness of the deployment of the new instrument. As part of the customary experiments: muscle activity related to different hand gestures were collected and analysed/visualised; both EMG and EEG recordings were collected enabling an experiment which allowed for a more integrated study of the motor nervous system (peripheral and central) and confirming the presence of cortico-muscular coherence in the range of 19-20Hz; based on W^2 Myolink recorded EMG signals, real-time decomposition of motor-unit action potentials for different finger- and hand- movements was achieved and visualised; and by means of the use of surrogate/played-back clinical/physiological data, it was confirmed that $W^2Myolink$ is indeed capable of recording and transmitting not only EMG data corresponding to healthy subjects but also EMG data corresponding to neuropathy, myopathy and Amyotrophic-Lateral-Sclerosis (ALS). As part of the more complex experiments: the successful deployment and collection of EMG data in human-robot-interaction experiments which involved ISYBOT robotic arms were confirmed; moreover, $W^2Myolink$ was deployed in the operating theatre enabling the collection and analysis of EMG data from the operating surgeon during different types of operation and for the cases that an exoskeleton is assisting (or not) the surgeon who performs the operation; finally the new device was deployed to collect EMG data during a psychedelic experience induced by psilocybin and confirmed the existence of specific spectral bands of higher beta band activity when compared against the baseline state.

Though the above experimental facts stress the usefulness of the new device, it should be highlighted that the modularity of the design, its low area profile, its high channel-count and the ability of the Wi-Fi protocol to support a high data payload, cumulatively, allows us to argue that the migration of the current design to a version that could support the collection and wireless transmission of not only EMG but also EEG signals is possible and of manageable risk. For example, one may consider a version of the device with customised (mostly gain and bandwidth) analogue front ends with, say, 64 channels dedicated to EMG collection and another, say, 64 channels dedicated to the collection of EEG signals from different bands (e.g. alpha beta, etc). Clearly such an approach would need to be accompanied by the adoption of the appropriate types of electrodes. Furthermore, the practical nature of the specific device allows for one to conceive natural movement involving experiments where multiple devices are attached to a person, or a collection of persons, each attached to/with a device and all together

being monitored while participating and interacting in an experiment. Admittedly, the data stream generated in such cases would be high, but the emergence of machine learning suggests that it should be possible to extract meaning from such large amounts of dynamic datasets. We believe that the new device presented here paves the way for such advanced experimental conceptions.

6. Acknowledgements

We acknowledge support and contributions by Rosalind McAlpine (UCL), Pedro Mediano (Imperial College London) and Jeremy Skipper (UCL) to the psychedelic experience monitoring experiment.

7. Data Access

Please contact the Lead or the Corresponding Author

8. Ethics

All above mentioned experiments were carried out with the consent of subjects and were founded in preexisiting ethical approvals where neccesary and essential. Additionally, extra ethical measures were considered at the time of each experiment through disuccsion and personal assessment to prevent miscommunication and consider additional ad hoc risks.

9. Funding

We acknowledge support by the NISNEM EPSRC Transformative Healthcare Technology Project (EP/T020970/1) and from the Dept. of Bioengineering- Imperial College London

[1] Frontiers in Neurorobotics, *Development of an EMG-Controlled Knee Exoskeleton to Assist Home Rehabilitation in a Game Context* (2019), https://doi.org/10.3389/fnbot.2019.00067

[2] Meta, *Inside Facebook Reality Labs: Wrist-based interaction for the next computing platform* (2022), https://tech.fb.com/ar-vr/2021/03/inside-facebook-reality-labs-wrist-based-interaction-for-the-next-computing-platform/

[3] J. Bashford, K. Mills, C. Shaw, *The evolving role of surface electromyography in amyotrophic lateral sclerosis: A systematic review* (2020), https://www.sciencedirect.com/science/article/pii/S1388245 719313732

[4] MillMed, *Understanding Surface EMG and High-Density Surface EMG* (2025), https://hillmedgroup.com/understanding-surface-emg-and-high-density-surface-emg/

[5] D. Farina, F. Negro, J. L. Dideriksen. *The effective neural drive to muscles is the common synaptic input to motor neurons* (2014), https://pubmed.ncbi.nlm.nih.gov/24860172/

[6] Y. Zheng and X. Hu, *Interference Removal From Electromyography Based on Independent Component Analysis* (2019), IEEE TRANSACTIONS ON NEURAL SYSTEMS AND REHABILITATION ENGINEERING, Volume: 27, Issue: 5, https://ieeexplore.ieee.org/stamp/stamp.jsp?arnumber=8688427&tag=1

[7] G. Hajian, A. Etemad, E. Morin, *Automated Channel Selection in High-Density sEMG for Improved Force Estimation* (2020), PubMed Central, PMCID: PMC7576492 PMID: 32867378, https://pmc.ncbi.nlm.nih.gov/articles/PMC7576492/

[8] E. Abbagnano, A. Pascual-Valdunciel, B. Zicher, J. Ibañez, D. Farina, *Projection of Cortical Beta Band Oscillations to a Motor Neuron Pool across the Full Range of Recruitment* (2025), The Journal of Neuroscience, https://spiral.imperial.ac.uk/server/api/core/bitstreams/b13a89e0-f4f1-4f4f-9515-562d60586a63/content

[9] OT Bioelettronica, *Quattrocento* (2025), https://otbioelettronica.it/en/quattrocento/

[10] OT Bioelettronica, *Muovi+* (2025), https://otbioelettronica.it/en/muoviplus/

[11] A. Moin, A. Zhou, A. Rahimi, S. Benatti, *An EMG Gesture Recognition System with Flexible High-Density Sensors and Brain-Inspired High-Dimensional Classifier* (2018), https://arxiv.org/pdf/1802.10237.pdf

[12] M. Zajaczkowski, S. Koutsoftidis, D. Farina, and E.M. Drakakis, *A Wearable 128-Channel Wireless Device for High-Density Surface Electromyography Recording* (2025), IEEE

[13] OT Bioelettronica, *Electrodes* (2025), https://otbioelettronica.it/en/product-category/electrodes/page/4/

[14] X. Jiang, X. Liu, J. Fan, X. Ye, C. Dai *Enhancing IoT Security via Cancelable HD-sEMG-based Biometric Authentication Password, Encoded by Gesture* (2021), IEEE internet of Things Journal, Volume: 8 Issue: 22, https://ieeexplore.ieee.org/document/9410579

[15] E. Nsugbe, C. Phillips, M. Fraser, J. McIntosh, *Gesture recognition for transhumeral prosthesis control using EMG and NIR*, The Institute of Engineering and Technology (2020), https://doi.org/10.1049/iet-csr.2020.0008

[16] A. Moin, A. Zhou, A. Rahimi, S. Benatti, *An EMG Gesture Recognition System with Flexible High-Density Sensors and Brain-Inspired High-Dimensional Classifier* (2018), https://arxiv.org/pdf/1802.10237.pdf

[17] C. Brambilla, I. Pirovano,, R. M. Mira, G. Rizzo, A. Scano, A. Mastropietro, *Combined Use of EMG and EEG Techniques for Neuromotor Assessment in Rehabilitative Applications: A Systematic Review* (2021), PubMed Central, Oct 22;21(21):7014, https://pmc.ncbi.nlm.nih.gov/articles/PMC8588321/

[18] E. Abbagnano,A. Pascual-Valdunciel, B. Zicher, J. Ibañez, D. Farina, *Projection of Cortical Beta Band Oscillations to a Motor Neuron Pool across the Full Range of Recruitment* (2025), The Journal of Neuroscience, Systems/Circuits,

45(31):e0453252025, https://spiral.imperial.ac.uk/server/api/core/bitstreams/b13a89e0-f4f1-4f4f-9515-562d60586a63/content

[19] M. Bracklein, D. Y Barsakcioglu, A. Del Vecchio, J. Ibanez, D. Farina, *Reading and Modulating Cortical β Bursts from Motor Unit Spiking Activity* (2022), The Journal of Neuroscience, Apr 27;42(17):3611–3621. doi: 10.1523/JNEUROSCI.1885-21.2022

[20] Grison, A., Mendez Guerra, I., Clarke, A.K., Muceli, S., Ibáñez, J. and Farina, D. (2025). *Unlocking the full potential of high-density surface EMG: novel non-invasive high-yield motor unit decomposition.* The Journal of Physiology, 603(8), pp.2281–2300. doi:https://doi.org/10.1113/jp287913.

[21] D. S. Oliveira , M. Ponfick , D. I Braun , M. Osswald, et al. *A direct spinal cord–computer interface enables the control of the paralysed hand in spinal cord injury, Brain, Volume 147, Issue 10, October 2024, Pages 3583–3595*, https://doi.org/10.1093/brain/awae088

[22] D. Y. Barsakcioglu, M. Bräcklein, A. Holobar and D. Farina, "Control of Spinal Motoneurons by Feedback From a Non-Invasive Real-Time Interface," in IEEE Transactions on Biomedical Engineering, vol. 68, no. 3, pp. 926-935, March 2021, doi: 10.1109/TBME.2020.3001942.

[23] D. Y. Barsakcioglu and D. Farina, "A real-time surface EMG decomposition system for non-invasive human-machine interfaces," 2018 IEEE Biomedical Circuits and Systems Conference (BioCAS), Cleveland, OH, USA, 2018, pp. 1-4, doi: 10.1109/BIOCAS.2018.8584659.

[24] D. A. Sherman, J. Rush, M. S. Stock, C. D. Ingersoll, G. E. Norte, *Neural drive and motor unit characteristics after anterior cruciate ligament reconstruction: implications for quadriceps weakness* (2023), Sports Medicine and Rehabilitation. https://peerj.com/articles/16261/

[25] J. A. Bashford, A. Wickham, R Iniesta, E. M. Drakakis, M. G. Boutelle, K. R. Mills and C. E. Shaw, *The rise and fall of fasciculations in amyotrophic lateral sclerosis* (2020), Brain Communications, Feb 20;2(1):fcaa018. doi: 10.1093/braincomms/fcaa018, https://pmc.ncbi.nlm.nih.gov/articles/PMC7425399/

[26] J. Yang, K. Shibata, D. Weber & Z. Erickson, *High-density electromyography for effective gesture-based control of physically assistive mobile manipulators* (2025), Nature NPJ Robotics, Volume 3, Article number: 2 (2025) , https://www.nature.com/articles/s44182-025-00018-3

[27] Y. Rivero-Moreno, S. Echevarria, C. Vidal-Valderrama, L. Pianetti 4, *Robotic Surgery: A Comprehensive Review of the Literature and Current Trends* (2023), Cureus Jul 24;15(7):e42370. doi: 10.7759/cureus.42370, https://pmc.ncbi.nlm.nih.gov/articles/PMC10445506/

[28] Mediano P., Rosas F., Luppi A., Noreika V., Seth A., Carhart-Harris R., Barnett L., Bor D. *Spectrally and temporally resolved estimation of neural signal diversity* (2023), https://elifesciences.org/reviewed-preprints/88683v1

[29] Y. Yao, D. Guo, T.-S. Lu, F. L. Liu, *Efficacy and safety of psychedelics for the treatment of mental disorders: A systematic review and meta-analysis* (2024), Psychiatry Research, Volume 335, May 2024, 115886, https://www.sciencedirect.com/science/article/pii/S0165178124001719

[30] Fernando E. Rosasa, P. A.M. Mediano, C. Timmermann, A. I Luppig, *The entropic heart: Tracking the psychedelic state via heart rate dynamics* (2023), BiorXiv, https://www.biorxiv.org/content/biorxiv/early/2023/11/09/2023.11.07.566008.full.pdf

[31] Matthew W. Flood, *EntropyHub An open-source toolkit for entropic data analysis* (2025), https://www.entropyhub.xyz/

[32] R. L. C.-Harris, R. Leech, P. J. Hellyer, M. Shanahan, *The entropic brain: a theory of conscious states informed by neuroimaging research with psychedelic drugs* (2014), Frontiers, https://www.frontiersin.org/journals/human-neuroscience/articles/10.3389/fnhum.2014.00020/full